



## Petrogenesis of the new Iherzolitic shergottite Grove Mountains 99027: Constraints of petrography, mineral chemistry, and rare earth elements

Yangting LIN<sup>1, 2\*</sup>, Yunbin GUAN<sup>3</sup>, Daode WANG<sup>2</sup>, Makoto KIMURA<sup>5</sup>, and Laurie A. LESHIN<sup>4</sup>

<sup>1</sup>State Key Laboratory of Lithosphere Tectonic Evolution, Institute of Geology and Geophysics, Chinese Academy of Sciences, P.O. Box 9825, Beijing 100029, China

<sup>2</sup>Guangzhou Institute of Geochemistry, Guangzhou 510640, China

<sup>3</sup>Department of Geological Sciences, Arizona State University, Tempe, Arizona 85287–1404, USA

<sup>4</sup>Center for Meteorite Studies, Arizona State University, Tempe, Arizona 85287–1404, USA

<sup>5</sup>Institute of Astrophysics and Planetary Science, Faculty of Science, Ibaraki University, Mito 310-8512, Japan

\*Corresponding author. E-mail: [Linyt@mail.igcas.ac.cn](mailto:Linyt@mail.igcas.ac.cn)

(Received 24 January 2005; revision accepted 05 August 2005)

**Abstract**—We report petrography, mineral chemistry, and microdistribution of rare earth elements (REE) in a new Iherzolitic shergottite, Grove Mountains (GRV) 99027. The textural relationship and REE patterns of minerals suggest precipitation of cumulus olivine and chromite, followed by equilibrium crystallization of a closed system with a bulk composition of the inferred intercumulus melt. Subsolidus equilibrium temperatures of pyroxenes and olivine range from 1100 to 1210 °C, based on a two-pyroxene thermometry and Ca partitioning between augite and olivine. Oxygen fugacity of the parent magma is 1.5–2.5 (av.  $2.0 \pm 0.4$ ) log units below the quartz-fayalite-magnetite (QFM) buffer at 960–1360 °C, according to the olivine-orthopyroxene-chromite barometer. The ilmenite-chromite barometer and thermometer show much wider ranges of oxygen fugacity (1.0–7.0 log unit below QFM) and temperature (1130–480 °C), suggesting subsolidus equilibration of the oxides at low temperatures, probably due to deep burial of GRV 99027 on Mars. The low oxygen fugacity and LREE depletion of the parent magma of GRV 99027 suggest low contamination by martian crust.

Characteristics of GRV 99027 demonstrate similarity of Iherzolitic shergottites, suggesting a high possibility of launch pairing or a homogeneous upper mantle of Mars if they were ejected by individual impact events. However, GRV 99027 probably experienced severe post-shock thermal metamorphism in comparison with other Iherzolitic shergottites, based on the re-crystallization of maskelynite, the homogeneity of minerals, and the low subsolidus equilibrium temperatures between chromite and ilmenite.

### INTRODUCTION

Shergottites are a subset of Martian meteorites, and are divided into three petrographic types: basaltic, Iherzolitic, and olivine-phyric. Basaltic shergottites consist predominantly of clinopyroxene (augite, pigeonite) and maskelynite (shock-produced diaplectic glass). Iherzolitic shergottites are olivine-pyroxene cumulates with low abundance of plagioclase. They comprise two petrographic lithologies, i.e., a poikilitic part, consisting of pigeonite oikocrysts with euhedral olivine and chromite inclusions, and an interstitial part, consisting of granular olivine, augite, and pigeonite, with interstitial plagioclase. Olivine-phyric shergottites have only recently been recognized (Goodrich 2002); they consist

of olivine megacrysts in fine-grained groundmass of clinopyroxene and plagioclase. In comparison with basaltic and olivine-phyric types, Iherzolitic shergottites are less abundant (6 versus 13 and 8, respectively). In addition, only three of them, i.e., Allan Hills (ALH) 77005, Yamato (Y-) 793605, and Lewis Cliff (LEW) 88516, have been extensively studied. The other three Iherzolitic shergottites, Grove Mountains (GRV) 99027 and 020090, and Northwest Africa (NWA) 1950, were reported recently, and only brief descriptions on petrography and mineralogy are available, with the exception of the recent ion probe study of GRV 99027 by Hsu et al. (2004).

The petrography, mineral chemistry, and geochemistry of ALH 77005, Y-793605, and LEW 88516 are very similar.

All of them consist of both poikilitic and interstitial lithologies with lower FeO contents of Mg-Fe-silicates in the poikilitic lithology than in the interstitial (McSween et al. 1979; Harvey et al. 1993; Treiman et al. 1994; Ikeda 1997; Mikouchi and Miyamoto 1997, 2000). Their similar bulk compositions (Boynton et al. 1992; Dreibus et al. 1992; Lindstrom et al. 1992; Treiman et al. 1994; Warren and Kallemeyn 1997), rare earth element (REE) patterns of minerals (Lundberg et al. 1990; Wadhwa et al. 1999), Rb-Sr and Sm-Nd isochron ages (Morikawa et al. 2001; Borg et al. 2002), and ejection ages (Nyquist et al. 2001; Eugster et al. 2002) suggest an identical igneous source on Mars. The similarities among Iherzolitic shergottites are significant, in comparison with the wide ranges of petrography, mineralogy, and chemical and isotopic compositions of the basaltic and olivine-phyric types, which are probably due to contamination by the Martian crust or derivation from different magmatic sources (e.g., Wadhwa 2001; Herd et al. 2002; Goodrich et al. 2003b; Warren and Bridges 2005).

GRV 99027 was recognized as the fourth Iherzolitic shergottite and shows similar petrography, mineralogy, and oxygen isotopes with ALHA77005, Y-793605, and LEW 88516 (Lin et al. 2002; Lin et al. 2003). Hsu et al (2004) recently reported ion probe analyses of REE in various constituent phases of GRV 99027, confirming the similarity of this specimen with other Iherzolites. The authors also noticed that GRV 99027 has relatively homogeneous mineral compositions and suggested that it suffered a higher degree of subsolidus equilibration than the other Iherzolitic shergottites. In this paper, we extend the study of GRV 99027, determine its parent magma, and clarify the crystallization conditions and sequence. In addition, we discuss the genetic linkage of GRV 99027 with other Iherzolitic shergottites. This work is based on a detailed combination of petrography, mineral chemistry, and microdistribution of REE in GRV 99027. The preliminary results were reported by Lin et al. (2002, 2003).

## SAMPLE AND EXPERIMENTS

GRV 99027 has a mass of 9.97 g, and most of the surface is covered by fusion crust. We broke off a 3.74 g fragment of the sample using a chisel and cut this subsample into five thin slices (~1 mm), numbering them from GRV 99027-1 to GRV 99027-5. In this study, we used the slice GRV 99027-3 and made it into a polished thin section ( $0.9 \times 1.3 \text{ cm}^2$ ). Petrographic observations were obtained with an optical microscope and backscattered electron (BSE) images taken with an electron probe microanalyzer (EPMA), type JXA 8800 at Zhongshan University, Guangzhou, China, and type JXA 733 at Ibaraki University, Japan. Quantitative analyses of minerals were carried out using the same EPMA using 15 kV accelerating voltage and 20 nA beam current (10 nA for analyses of plagioclase). Bulk compositions of melt pockets and magmatic inclusions were analyzed with a

method described by Lin and Kimura (2003), using a defocused beam 50  $\mu\text{m}$  in diameter for the pockets and 10  $\mu\text{m}$  in diameter for the inclusions. We corrected X-ray overlapping of  $K_\alpha$  lines of Mn and V by  $K_\beta$  lines of Cr and Ti, respectively, using a deconvolution program, and treated the analyses using the Bence-Albee method. The detection limits are ( $1\sigma$ ) 0.01 wt% for  $\text{K}_2\text{O}$ , 0.02 wt% for  $\text{SiO}_2$ ,  $\text{Al}_2\text{O}_3$ ,  $\text{V}_2\text{O}_5$ ,  $\text{MgO}$ ,  $\text{CaO}$ ,  $\text{Na}_2\text{O}$ ,  $\text{P}_2\text{O}_5$ , and  $\text{Cl}$ , 0.03 wt% for  $\text{TiO}_2$  and  $\text{Cr}_2\text{O}_3$ , 0.05 wt% for  $\text{FeO}$ , 0.06 wt% for  $\text{NiO}$  and  $\text{MnO}$ , and 0.15 wt% for  $\text{SO}_3$ . Modal composition of the section was calculated from surface areas of individual minerals on the BSE mosaic image. Grain size distribution and orientation of olivine were determined from the same mosaic using a graphics software.

We determined the microdistribution of REEs in the sample with a Cameca-6f ion microprobe at Arizona State University, using the energy filtering technique that was described by Zinner and Crozaz (1986). An  $\text{O}^-$  primary ion beam of  $-12.5 \text{ keV}$ , ranging from 1 to 4 nA, was focused to  $<20 \mu\text{m}$  in diameter onto the sample surface. Secondary ions, offset from a nominal  $+10 \text{ keV}$  accelerating voltage by  $-100 \text{ keV}$ , were collected in peak-jumping mode with an electron multiplier. To increase the transmission of the secondary ion signals, an imaged field of  $\sim 75 \mu\text{m}$  was used. Total counting time varied from  $\sim 30 \text{ min}$  to  $\sim 4 \text{ hr}$ , depending on the phases analyzed. For the analyses of olivine with low LREE contents, we discarded the data from the first few cycles of the counting, which shows the highest La and indicates possible surface contamination or terrestrial weathering. Silicon and calcium were used as the reference elements for silicates and phosphates, respectively. NBS-610, NBS-612, synthetic titanium-pyroxene glass, and Durango apatite standards were measured periodically to account for any variation of ionization efficiencies caused by minor changes of operating conditions.

## RESULTS

### Petrography

The polished thin section in this study contains two lithologies (Fig. 1). The more abundant lithology (60.7 vol%) has a poikilitic texture, with euhedral olivine and chromite embedded in a megacryst of pigeonite. The olivine chadacrysts are usually rounded (Fig. 2a). The non-poikilitic lithology (39.3 vol%) consists mainly of euhedral to subhedral olivine, pigeonite, and augite with interstitial plagioclase (Fig. 2b), and is hereafter referred to as the interstitial lithology. We found no exsolution of pyroxenes in either lithology. In fact, augite overgrows along the boundaries of the pigeonite oikocrysts or as large subhedral grains in the interstitial lithology. Except for chromite in both lithologies, other minor phases (i.e., merrillite and ilmenite) are confined to the interstitial lithology and show a close

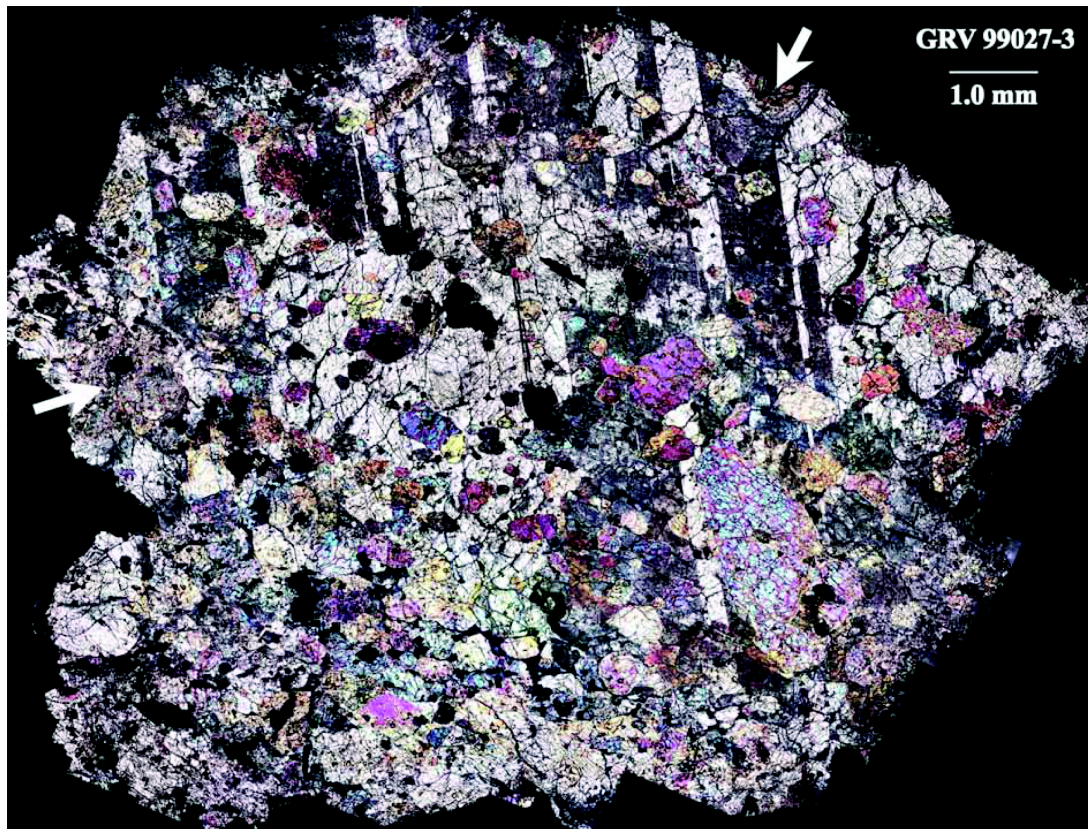


Fig. 1. Photo mosaics of GRV 99027 in cross-polarized light. The upper part is a megacryst of pigeonite, showing lamellae twins and enclosing many olivines. The lower part is non-poikilitic, consisting of olivine, augite, and pigeonite with interstitial plagioclase. Two shock-induced melt pockets (arrows) are visible.

spatial relationship with plagioclase (Figs. 2b and 2c). The modal compositions of each lithology and the whole section are listed in Table 1. The modal abundances of olivine and chromite in the poikilitic part are nearly identical to those in the interstitial one. We calculated the bulk compositions of each lithology and the whole section based on the modal compositions and average mineral chemistry (Table 2).

Crystals of olivine and chromite in both lithologies show preferred orientation as referenced to the long dimension of the grains. From the BSE photo mosaic, we analyzed only the orientation of olivine, i.e., angles between the long axis of olivine grains and the long side of the section. It is evident that the olivine in both the poikilitic and interstitial lithologies shows identical orientation patterns (Fig. 3a). In addition, we also measured the sizes of olivine grains from the same photo mosaic, revealing their identical size distribution patterns in both lithologies (Fig. 3b). The natural logarithm of the number of olivine grains is negatively correlated with the size, except for an overturn at the smallest size fraction. The average size of olivine grains is  $230 \pm 140 \mu\text{m}$ .

We observed two shock-induced melt pockets (1.1 mm and  $\geq 0.6$  mm in diameter, respectively) in the section (Fig. 1). They are recrystallized and consist mainly of lath-like olivine, low-Ca pyroxene, and Ca-pyroxene with minor interstitial

feldspathic mesostasis. Heterogeneity in the small crystals can be noticed in their BSE images, which usually have dark (MgO-rich) cores and bright (FeO-rich) rims. We measured bulk compositions of the melt pockets using the defocused beam method; the results are given in Table 2. Besides the melt pockets, other shock features include intense fractures and common undulose and mosaic extinctions of olivine and pyroxenes. Plagioclase is usually anisotropic in polarized light and thus is not maskelynite. It often contains numerous fine laths of Mg-Fe silicates, especially along boundaries in contact with other silicates (Fig. 2c). Plagioclase commonly contains bubble-like voids with smooth surfaces and round shapes, and has fine veins injected into the neighboring phases (Fig. 2b).

Small magmatic inclusions (30–60  $\mu\text{m}$  in diameter) were found in the olivine (Fig. 4), but none were observed in the pyroxene oikocrysts. The absence of magmatic inclusions in the oikocrysts is confirmed by observation of GRV 020090, which was found in the same Grove Mountain region. The magmatic inclusions in olivine are round or ovoid in shape, consisting predominantly of feldspar glass with minor pyroxene as dendritic grains embedded in the glass matrix and/or as thin rims along the walls of inclusions. A few inclusions contain minor dark and  $\text{SiO}_2$ -rich grains (probably

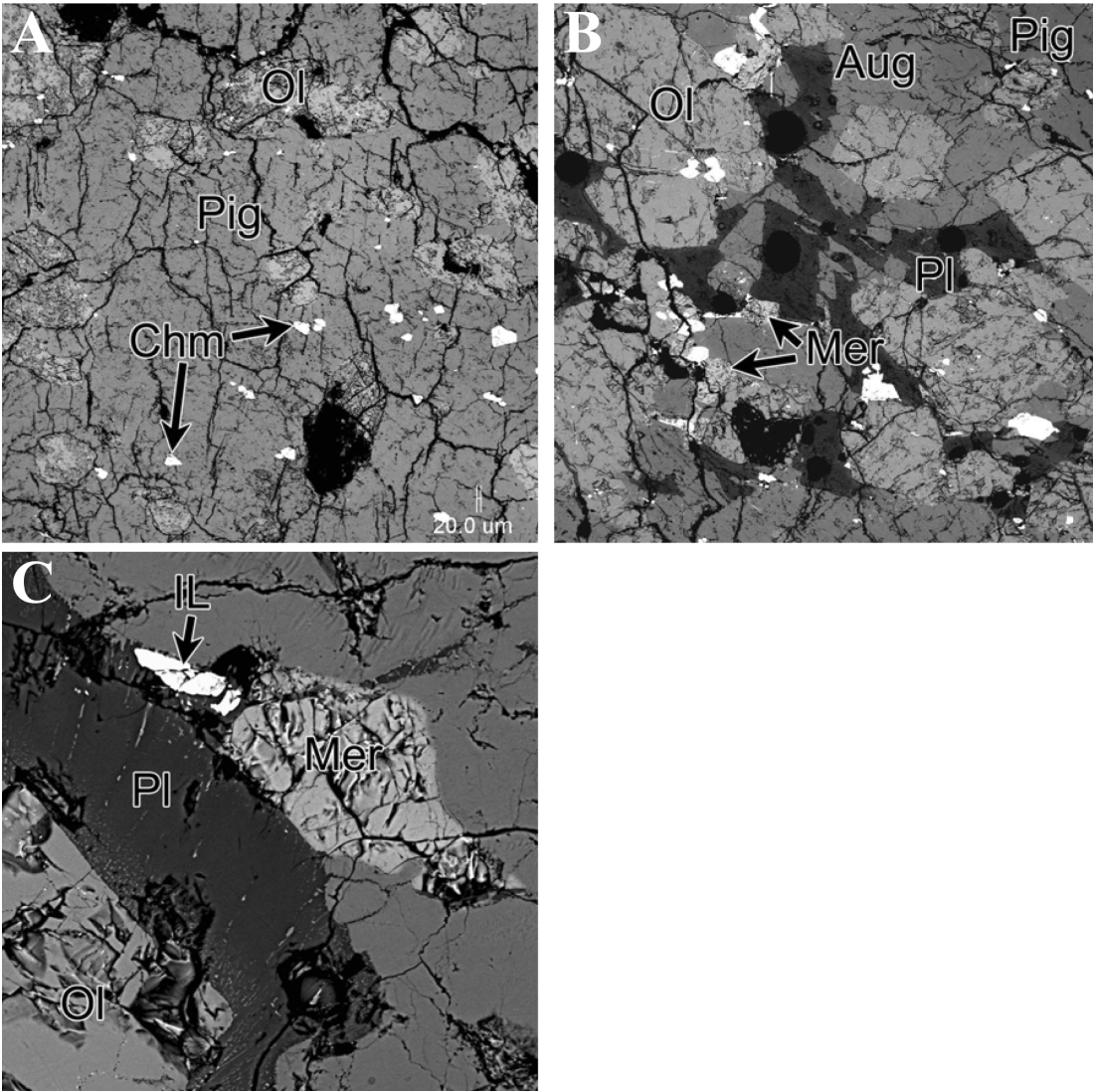


Fig. 2. Backscattered electron (BSE) images of GRV 99027. a) Poikilitic texture, showing rounded olivine (Ol) and euhedral chromite (Chm) in the pigeonite (Pig) oikocryst. Note the fractures in the olivine and pigeonite. Width of the view is 2.4 mm. b) Interstitial texture, consisting of euhedral to subhedral olivine, pigeonite and augite (Aug) with interstitial plagioclase (Pl). Note the dark and bubble-like voids in the plagioclase, and the fine veins of plagioclase injected into the neighboring silicates. Minor phases are chromite-ilmenite (white) and merrillite (Mer). Width of the view is 1.7 mm. c) Plagioclase shows thin lamellae along the boundaries. Abbreviation: Il (ilmenite). Width of the view is 140  $\mu\text{m}$ .

a silica polymorph). Only one inclusion in the largest olivine chadacryst is full crystalline, consisting of Ca-rich and Ca-poor pyroxenes without feldspar glass (Fig. 4c). This inclusion has a highly elongated shape that is different from the others. Bulk compositions of the magmatic inclusions, determined using the defocused beam method, are reported in Table 2.

**Major and Minor Elements of Minerals**

*Olivine*

The composition of olivine is correlated with the textural setting (Fig. 5). The grains in the poikilitic lithology contain

Table 1. Modal compositions of GRV 99027, normalized to 100 vol%.

	Poikilitic (60.7%)	Interstitial (39.3%)	Bulk
Olivine	30.9	33.9	32.1
Orthopyroxene	66.4	38.3	55.4
Ca-pyroxene	1.4	10.4	5.0
Chromite	1.2	0.9	1.1
Ilmenite	–	+	+
Plagioclase	–	14.6	5.8
Merrillite	–	1.4	0.5
Sulfides	–	0.4	0.2

+ : minor; – : not found.



Table 2. Compositions of bulk GRV 99027, the inferred intercumulus melt, shock melt pockets, and magmatic inclusions, normalized to 100 wt%.

	Melt pocket		Magmatic inclusion in olivine					Inferred bulk compositions <sup>a</sup>			
	1	2	3	4	5	6	7	8	9	10	11
SiO <sub>2</sub>	38.6	44.1	51.6	61.4	62.4	60.4	60.5	47.2	48.7	48.1	54.5
TiO <sub>2</sub>	0.41	0.21	0.47	1.14	1.02	1.34	1.23	0.32	0.09	0.18	0.20
Al <sub>2</sub> O <sub>3</sub>	2.72	1.46	2.33	15.1	15.8	14.2	14.4	3.85	0.53	1.83	2.65
Cr <sub>2</sub> O <sub>3</sub>	1.50	1.26	1.09	n.d.	n.d.	n.d.	n.d.	0.77	1.22	1.04	0.36
FeO	22.8	21.0	11.6	4.31	3.70	4.84	5.58	16.7	17.2	17.0	13.0
NiO	0.11	0.10	n.d.	n.d.	n.d.	n.d.	n.d.	n.d.	n.d.	n.d.	n.d.
MnO	0.49	0.46	0.41	0.08	0.07	0.07	0.12	0.45	0.48	0.47	0.45
MgO	29.8	28.5	21.2	2.55	2.39	2.10	2.77	23.7	28.6	26.7	21.6
CaO	2.60	2.14	10.6	10.4	9.40	12.3	11.0	5.77	3.15	4.18	6.34
Na <sub>2</sub> O	0.61	0.37	0.34	3.45	3.98	3.29	2.73	0.71	0.04	0.30	0.47
K <sub>2</sub> O	0.03	0.09	0.04	0.10	0.19	0.12	0.07	0.01	n.d.	0.01	0.01
P <sub>2</sub> O <sub>5</sub>	0.11	n.d.	0.16	1.47	0.95	1.26	1.44	0.79	n.d.	0.31	0.47
SO <sub>3</sub>	n.d.	0.20	n.d.	n.d.	n.d.	n.d.	n.d.				
Cl	0.06	0.07	0.03	0.03	0.03	0.04	0.04				
Fe <sub>2</sub> O <sub>3</sub> <sup>b</sup>								0.04	0.04	0.04	0.01

<sup>a</sup>Calculated from the modal abundances and the average compositions of minerals.

<sup>b</sup>Contributed from chromite. 8: interstitial lithology; 9: poikilitic lithology; 10: bulk meteorite; 11: intercumulus melt. n.d.: below detection limit.

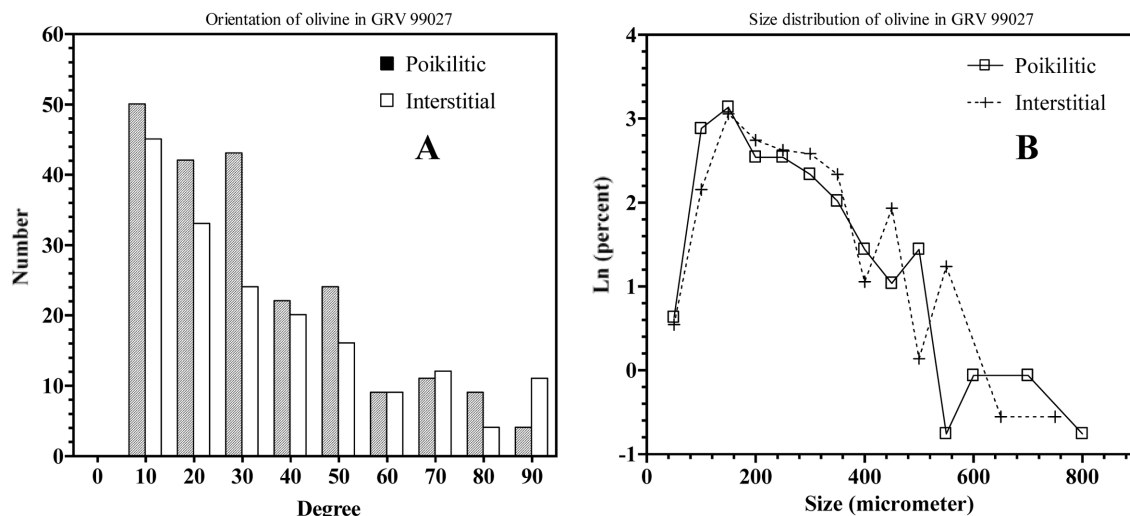


Fig. 3. Histograms of the orientation and size distribution of olivine grains. a) A histogram of olivine orientation showing similar patterns of the two lithologies. The orientation degree is the angle between the long dimensions of olivine grains and the section. b) Size distribution patterns of olivine showing similar patterns of the two lithologies. The natural logarithm of the number of olivine grains is negatively correlated with the size, except for a drop at the smallest size fraction.

lower fayalite (Fa) component (av.  $26.8 \pm 1.3$  mol%) than those in the interstitial part (av.  $29.3 \pm 0.8$  mol%). However, EPMA profiles and analyses of the rims and cores of large olivine grains in both lithologies show relatively homogeneous compositions (Table 3). In contrast, the small laths of olivine in the melt pockets are highly zoned, with Fa content increasing from 17.2 to 34.5 mol% toward the rims. The average composition of olivine in the melt pockets (av.  $26.3 \pm 4.1$  mol% Fa) is similar to that of the grains in the poikilitic lithology where the pockets are located. The average Mn/Fe atomic ratio of olivine ( $0.48 \pm 0.05$ ) is nearly the same for all of the three occurrences. All olivine grains

contain minor CaO (0.06–0.35 wt%, except for 5 of 117 analyses with 0.41–0.69 wt%). Al<sub>2</sub>O<sub>3</sub>, Cr<sub>2</sub>O<sub>3</sub>, and NiO are below or close to the detection limits.

#### Pigeonite

Similar to olivine, pigeonite shows a correlation between textural setting and composition, with the grains in the interstitial lithology being more FeO-rich ( $24.5 \pm 1.3$  mol% Fs) than those in the poikilitic part ( $21.3 \pm 1.0$  mol% Fs). Figure 6 demonstrates a compositional gap of pigeonite between both occurrences, except for a few analyses of the interstitial lithology overlapping within the poikilitic range.

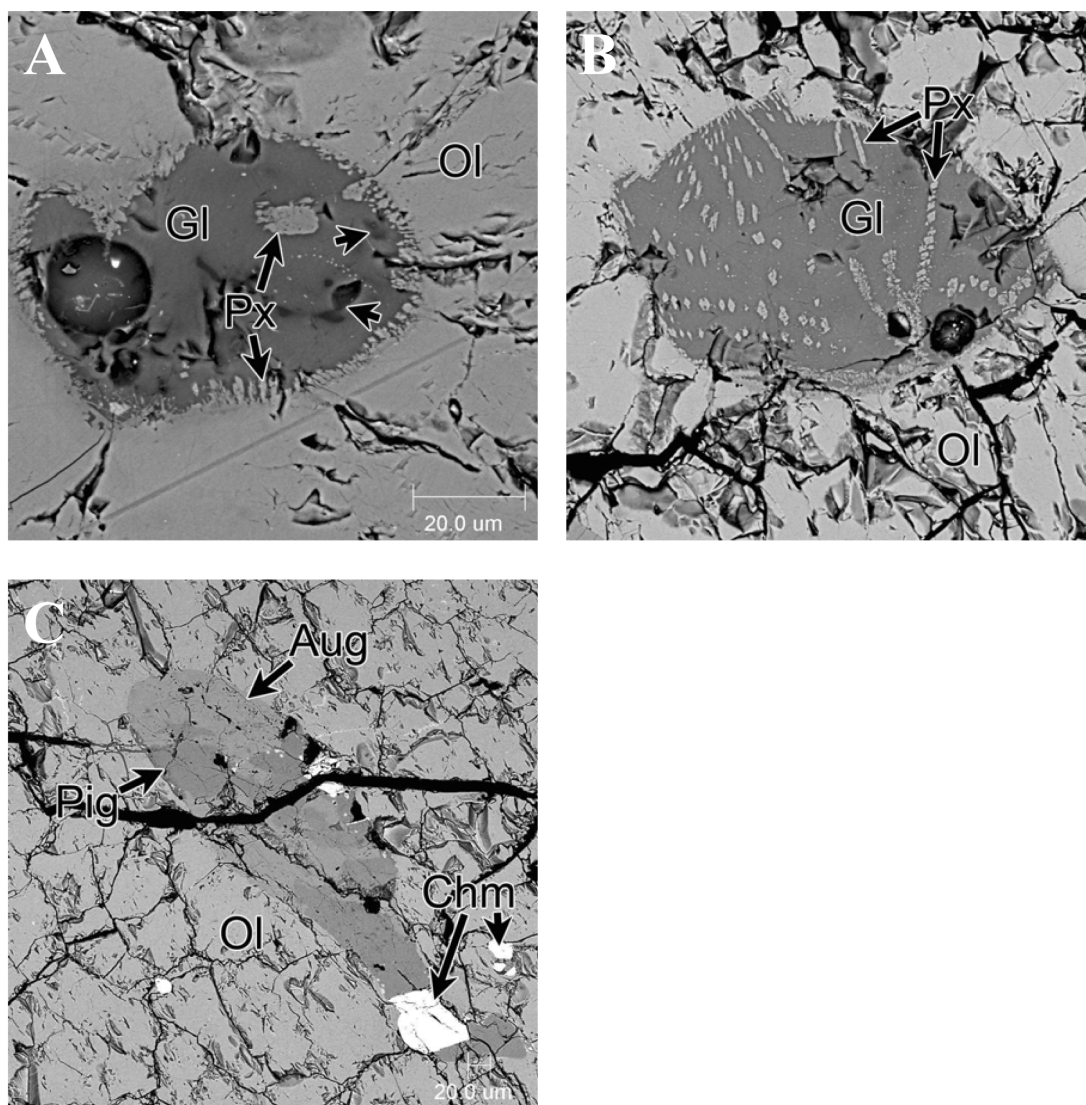


Fig. 4. BSE images of magmatic inclusions in olivine (Ol) in GRV 99027. a) A magmatic inclusion consisting of predominantly feldspar glass (Gl) with minor dendritic pyroxene (Px) along the periphery and a grain in the glass. Several tiny dark grains (arrows) in the glass are a silica mineral. On the left side, there is a large and round void. Width of the view is 100  $\mu\text{m}$ . b) Another magmatic inclusion with dendritic pyroxene mainly in the feldspar glass. Width of the view is 160  $\mu\text{m}$ . c) A crystalline magmatic inclusion, consisting of Ca-rich (Aug) and Ca-poor (Pig) pyroxenes. It has an elongated shape. Width of the view is 480  $\mu\text{m}$ .

Minor elements such as  $\text{Al}_2\text{O}_3$  and  $\text{TiO}_2$  are also higher in the interstitial lithology than in the poikilitic, but reverse for  $\text{Cr}_2\text{O}_3$  (Fig. 7). The CaO content is indistinguishable between both occurrences, although the poikilitic lithology has a wider range (1.46–8.46 wt%) than that of the interstitial (3.14–7.69 wt%). The  $\text{Al}_2\text{O}_3$  content seems positively correlated with those of CaO and  $\text{TiO}_2$  in the poikilitic lithology, but this is not the case for the interstitial region. Analyses of the cores and rims of pigeonite in both lithologies do not reveal significant zoning features. Although grains contain higher FeO in the interstitial lithology, there is no significant increase of FeO content of the oikocrystic pigeonite toward rim (Fig. 8). Representative analyses of pigeonite are given in Table 4.

#### Augite

Only a few grains of augite were found in the poikilitic region, and their compositions are indistinguishable from those in the interstitial region (Fig. 6). This is also the case for minor elements including  $\text{Al}_2\text{O}_3$ ,  $\text{TiO}_2$ ,  $\text{Cr}_2\text{O}_3$ , and MnO (Table 4). Figure 8 is an EPMA profile across augite at the interface of the two lithologies. It shows a slight decrease of Wo content toward the poikilitic pigeonite. This decreasing trend is more evident for the  $\text{Al}_2\text{O}_3$  content. In contrast, the Fs content is near constant.

#### Plagioclase

In spite of significant variation among grains of plagioclase ( $\text{An}_{42-61}$ ), analyses of the rims and cores of 14

Table 3. Representative analyses of olivine, wt%.

	Interstitial				Poikilitic				Shock melt pocket		
	1 <sup>a</sup>	2 <sup>b</sup>	3 <sup>a</sup>	4 <sup>b</sup>	5 <sup>a</sup>	6 <sup>b</sup>	7 <sup>a</sup>	8 <sup>b</sup>	9 <sup>a</sup>	10	11 <sup>b</sup>
SiO <sub>2</sub>	37.9	37.6	38.0	38.1	38.8	38.2	38.4	38.3	39.8	37.9	37.7
Al <sub>2</sub> O <sub>3</sub>	n.d.	n.d.	n.d.	n.d.	n.d.	n.d.	n.d.	n.d.	0.17	0.10	0.18
Cr <sub>2</sub> O <sub>3</sub>	n.d.	0.04	n.d.	n.d.	n.d.	n.d.	n.d.	n.d.	0.52	0.61	0.45
FeO	26.2	26.1	24.8	25.2	22.8	22.2	25.5	25.3	16.2	25.8	30.1
MnO	0.50	0.56	0.52	0.51	0.50	0.34	0.54	0.59	0.33	0.54	0.60
MgO	35.1	35.0	34.9	35.1	38.7	38.8	37.2	37.1	43.8	36.2	32.0
CaO	0.16	0.11	0.29	0.16	0.14	0.06	0.21	0.16	0.26	0.17	0.34
Total	99.8	99.4	98.4	99.0	100.9	99.6	101.9	101.4	101.1	101.3	101.4
Cation per 4 oxygen											
Si	1.006	1.004	1.017	1.015	1.003	0.998	0.995	0.997	0.995	0.991	1.005
Al	0.000	0.000	0.000	0.000	0.000	0.000	0.000	0.000	0.005	0.003	0.006
Cr	0.000	0.001	0.001	0.000	0.000	0.000	0.000	0.000	0.010	0.013	0.010
Fe	0.582	0.583	0.554	0.561	0.491	0.484	0.553	0.550	0.339	0.565	0.672
Ni	0.001	0.001	0.002	0.001	0.000	0.000	0.000	0.000	0.000	0.000	0.000
Mn	0.011	0.013	0.012	0.012	0.011	0.007	0.012	0.013	0.007	0.012	0.014
Mg	1.391	1.392	1.391	1.394	1.489	1.511	1.439	1.438	1.633	1.413	1.273
Ca	0.004	0.003	0.008	0.004	0.004	0.002	0.006	0.004	0.007	0.005	0.010
Fa mol%	29.5	29.5	28.5	28.7	24.8	24.3	27.8	27.7	17.2	28.5	34.5

<sup>a</sup>Core.<sup>b</sup>Rim.

n.d.: below the detection limit.

large grains, and EPMA profiles conducted on two other laths do not reveal any chemical zoning. The plagioclase contains very little orthoclase component (Or<sub>0.2–1.9</sub>). Minor FeO (0.19–0.93 wt%) and MgO (0.07–0.86 wt%) abundances are correlated and could be due to presence of the very thin laths of Mg-Fe-silicates as shown in Fig. 2c. However, the MgO/FeO ratio is much lower than that of the pyroxenes or olivine, suggesting of indigenous FeO content in plagioclase. The representative analyses are listed in Table 5.

### Chromite

The composition of chromite is also related to the textural setting (Fig. 9; Table 6). In the poikilitic lithology, chromite inclusions in both olivine and pigeonite are TiO<sub>2</sub>-poor (0.81–1.64 wt%), except for two large grains in the pigeonite, which are zoned with TiO<sub>2</sub>, Al<sub>2</sub>O<sub>3</sub>, and FeO increasing from core to rim (Fig. 10a). Chromite has on average higher Al<sub>2</sub>O<sub>3</sub> in olivine chadacrysts (10.2 ± 1.03 wt%) than in pigeonite oikocryst (7.29 ± 1.05 wt%). These analyses plot parallel to the join line between the Cr and Al apexes in the Cr-Al-Ti diagram (Fig. 9).

The small, round chromite inclusions in olivine in the interstitial region are TiO<sub>2</sub>-poor, similar to their counterparts in the poikilitic region. In contrast, other grains of chromite in the interstitial region are TiO<sub>2</sub>-rich and show a different trend in the Cr-Al-Ti triangle diagram (Fig. 9). In addition, they contain higher FeO than the grains in the poikilitic region (Fig. 11). Some large grains are highly zoned with TiO<sub>2</sub>-poor cores and TiO<sub>2</sub>-rich rims (Fig. 10b). Their Al<sub>2</sub>O<sub>3</sub>, MgO, and FeO contents, and the calculated Fe<sup>3+</sup>/ΣFe ratios based on

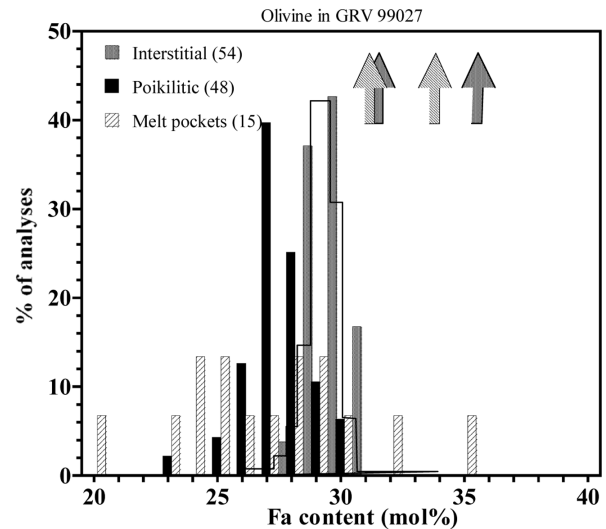


Fig. 5. Histogram of Fa content of olivine, showing a bimodal pattern with higher Fa content in the interstitial lithology than in the poikilitic. Range of ALHA77005 (outline) and peak positions of Y-793605 (hatched arrows) and LEW 88516 (dotted arrows) after Harvey et al. (1993), Treiman et al. (1994), and Ikeda (1997).

stoichiometry of chromite also increase from the core to the rim.

### Ilmenite

The major chemistry of ilmenite is rather homogeneous within and among grains. Besides FeO (36.2 ± 0.8 wt%) and TiO<sub>2</sub> (54.0 ± 0.6 wt%), ilmenite contains minor MgO (6.13–

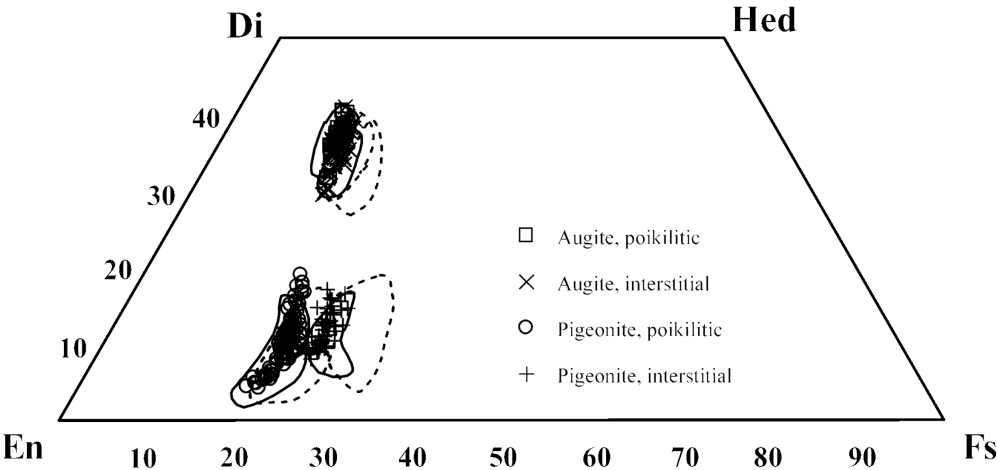


Fig. 6. Compositions of pyroxenes plotted in the enstatite-diogenite-ferrosilite-hedenbergite (En-Di-Fs-Hed) quadrangular diagram. Pigeonite has a distinguishable gap between interstitial and poikilitic lithologies, with higher FeO content in the former than the latter. In contrast, the compositions of augite of both occurrences overlap with each other. Ranges of ALHA77005 (thin line) and Y-793605 and LEW 88516 (dotted line) after Mikouchi and Miyamoto (2000).

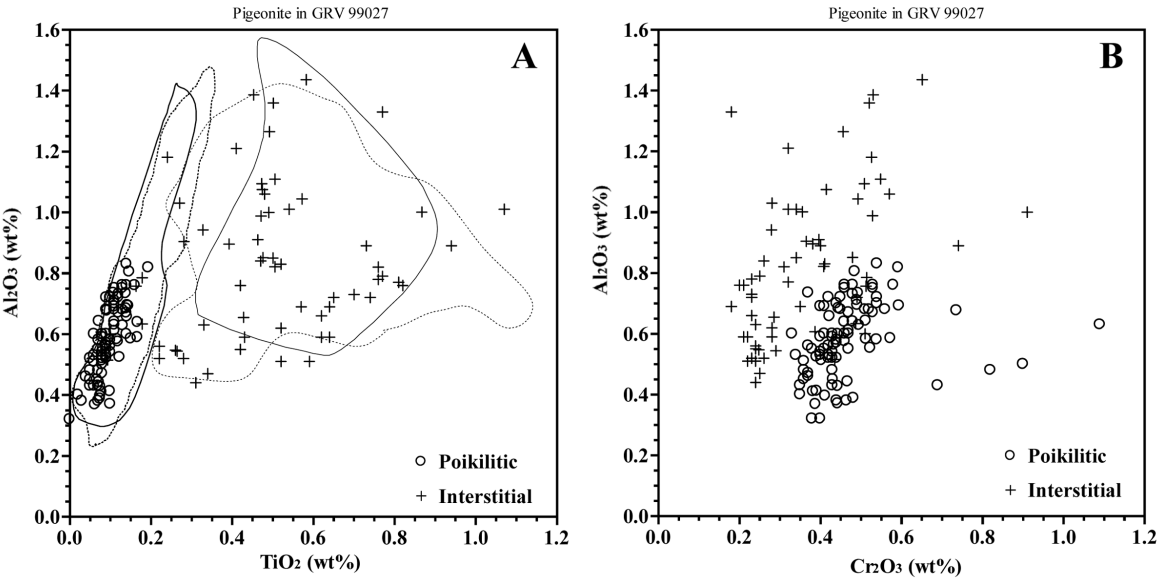


Fig. 7. Compositions of pigeonites. a)  $\text{Al}_2\text{O}_3$ - $\text{TiO}_2$  plot of pigeonite. The oikocrystic pigeonite shows positive correlation between  $\text{Al}_2\text{O}_3$  and  $\text{TiO}_2$ , with the lowest  $\text{TiO}_2$  content distinct from the other grains in the interstitial lithology. Ranges of ALHA77005 (thin line) and Y-793605 and LEW 88516 (dotted line) after Mikouchi and Miyamoto (2000). b)  $\text{Al}_2\text{O}_3$ - $\text{Cr}_2\text{O}_3$  plot of pigeonite, showing distinct compositions of the two occurrences.

7.98 wt%),  $\text{Al}_2\text{O}_3$  (0.09–0.32 wt%),  $\text{Cr}_2\text{O}_3$  (0.52–1.68 wt%),  $\text{MnO}$  (0.44–0.73 wt%),  $\text{CaO}$  (<0.68 wt%), and  $\text{V}_2\text{O}_5$  (<0.21 wt%). Representative data are listed in Table 6.

**Merrillite**

Merrillite has homogeneous composition and contains  $45.9 \pm 0.3$  wt%  $\text{CaO}$ ,  $45.6 \pm 0.4$  wt%  $\text{P}_2\text{O}_5$ ,  $3.65 \pm 0.11$  wt%  $\text{MgO}$ , and  $1.80 \pm 0.18$  wt%  $\text{FeO}$  with minor  $\text{Na}_2\text{O}$  ( $0.58 \pm 0.14$  wt%). Atomic  $\text{Fe}/(\text{Fe} + \text{Mg})$  ratio is  $0.22 \pm 0.02$  (lower

than Zagami:  $0.41 \pm 0.04$ ). Representative analyses are listed in Table 5.

**REE and Other Trace Elements**

**Olivine**

We analyzed the cores of large olivine chadacrysts that contain no magmatic inclusions. The REE pattern decreases continuously from HREE to LREE (Table 7; Fig. 12a), with



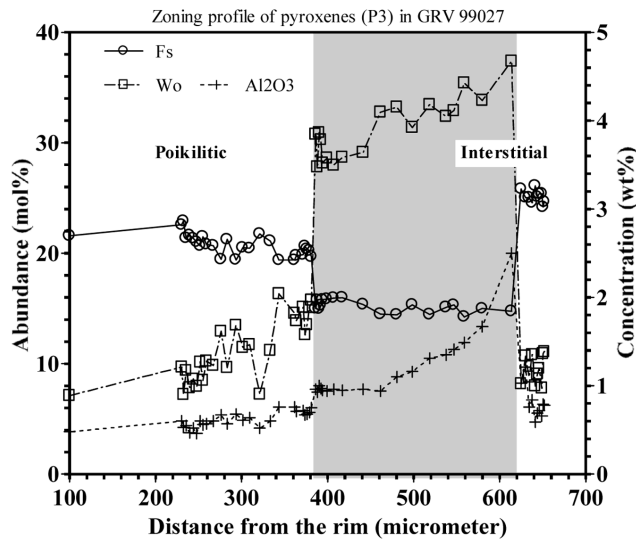


Fig. 8. EPMA profile of pyroxene. The pigeonite oikocryst shows a trend with Fs content decreasing and Wo and  $\text{Al}_2\text{O}_3$  contents increasing toward augite at the boundary between the two textural lithologies. The Wo and  $\text{Al}_2\text{O}_3$  contents of augite increase from one side in contact with the oikocryst to the other side, and the Fs content is nearly constant. Note the distinctly higher Fs content of pigeonite in the interstitial lithology. Fs and Wo contents are relative to the left axis, and  $\text{Al}_2\text{O}_3$  content is to the right one.

CI-normalized ratios of La/Dy and Yb/Dy of 0.11 and 1.5, respectively. Eu may have a slightly negative anomaly, but Sm shows a large analysis error.

#### Pigeonite

The REE patterns of pigeonite are similar to those of other ilherzolitic shergottites, and the REE concentrations are correlated with the petrographic setting (Table 7; Fig. 12b). The core of the oikocryst has the lowest REE without negative Eu anomaly ( $\text{Eu}/\text{Eu}^* = 1.2\text{--}1.8 \times \text{CI}$ ,  $\text{Eu}^*$  interpolated between Sm and Gd). The REE concentrations increase at the rims of the oikocryst, with relatively flat HREE patterns and no significant Eu anomaly either ( $\text{Eu}/\text{Eu}^* = 0.9 \times \text{CI}$ ). In contrast, other grains coexisting with plagioclase and augite in the interstitial lithology are the most REE-enriched. They have flat HREE patterns, with pronounced negative Eu anomalies ( $\text{Eu}/\text{Eu}^* = 0.7 \times \text{CI}$ ). Most analyses show an upward deflection at La. However, this could be an indication of surface contamination of terrestrial weathering because of the very low La abundances.

#### Augite

All analyses of augite show very similar REE patterns, but the abundances increase from core to rim or from the side in contact with oikocrystic pigeonite toward the interstitial lithology (Fig. 12c). Negative Eu anomalies are common, but small ( $\text{Eu}/\text{Eu}^* = 0.7\text{--}0.9 \times \text{CI}$ ). Slight decrease from Dy to Lu is noted. Augite in the largest and re-crystallized magmatic inclusion shows a more significant drop from Dy to Lu ( $\text{Lu}/\text{Dy}$

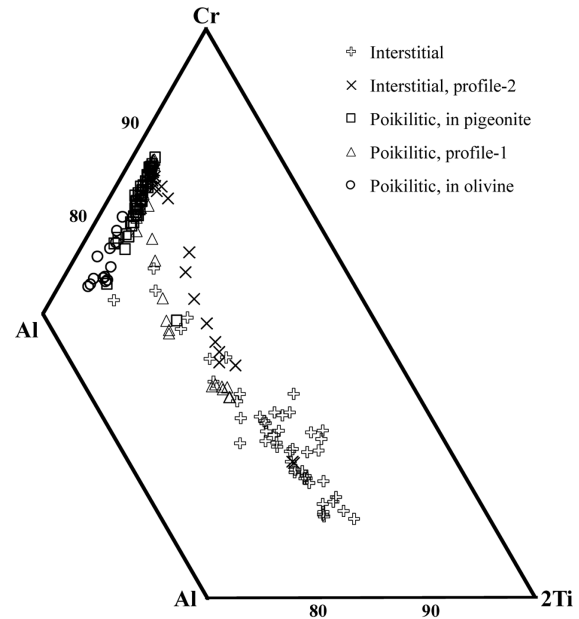


Fig. 9. Al-Ti-Cr atomic ratio plot of chromite. The grains in the poikilitic lithology are Ti-poor, distinguished from the Ti-rich grains in the interstitial region. Also notice higher Al content of chromite in olivine chadacrysts than that of the grains in pigeonite oikocryst. Two EMPA profiles are also plotted for comparison.

$= 0.33 \times \text{CI}$ ) in comparison with other grains ( $0.52\text{--}0.82 \times \text{CI}$ ).

#### Plagioclase

Plagioclase has a homogeneous composition of REEs and other trace elements, and shows a pronounced positive Eu anomaly ( $\text{Eu}/\text{Gd} = 37\text{--}63 \times \text{CI}$ ). The LREE concentration is higher than maskelynite in other ilherzolites (Fig. 12a).

#### Merrillite

Merrillite is the most REE-rich phase with concentrations of  $180\text{--}400 \times \text{CI}$ . The REE patterns are hump-shaped, decreasing from Dy to both La and Lu (Fig. 12d). No significant Eu-anomaly was found ( $\text{Eu}/\text{Eu}^* = 0.95\text{--}1.01 \times \text{CI}$ ).

#### Magmatic inclusions

The REE patterns of magmatic inclusions are similar to that of merrillite, but with much lower concentrations ( $2\text{--}30 \times \text{CI}$ ) and small positive or negative Eu-anomaly (Fig. 12d). The hump-shaped feature is more pronounced in the inclusions with lower REE concentrations. The representative analysis is given in Table 7.

## DISCUSSION

### Magmatism in the Martian Lithosphere

#### Crystallization Sequence of GRV 99027

GRV 99027 is a cumulate, as indicated by the preferred orientation of olivine grains. The rounded outlines of olivine

Table 4. Representative compositions of pyroxenes in GRV 99027, wt%.

	Augite								Pigeonite							
	Poikilitic				Interstitial				Poikilitic				Interstitial			
	1 <sup>a</sup>	2 <sup>b</sup>	3 <sup>a</sup>	4 <sup>b</sup>	5 <sup>a</sup>	6 <sup>b</sup>	7 <sup>a</sup>	8 <sup>b</sup>	9 <sup>a</sup>	10	11	12 <sup>b</sup>	13 <sup>a</sup>	14 <sup>b</sup>	15	16
SiO <sub>2</sub>	52.9	52.7	53.0	52.7	53.0	53.1	52.9	52.9	55.2	55.1	53.7	53.2	53.4	54.3	53.5	54.3
TiO <sub>2</sub>	0.24	0.49	0.26	0.34	0.27	0.32	0.41	0.47	0.07	0.08	0.07	0.08	0.57	0.51	0.87	0.47
Al <sub>2</sub> O <sub>3</sub>	1.26	2.04	1.37	1.41	1.25	1.35	1.84	2.02	0.45	0.40	0.64	0.60	1.04	0.82	1.00	1.08
Cr <sub>2</sub> O <sub>3</sub>	0.79	0.86	0.93	0.92	0.75	0.78	0.89	0.81	0.43	0.41	0.51	0.44	0.49	0.41	0.36	0.41
V <sub>2</sub> O <sub>3</sub>	0.08	0.08	0.03	0.08	0.04	0.12	0.10	0.13	n.d.	0.03	0.04	0.02	0.04	0.06	n.d.	n.d.
FeO	8.33	8.86	7.90	7.93	9.19	9.32	9.96	10.2	14.4	14.3	14.1	14.8	14.9	15.7	17.0	15.3
MnO	0.36	0.33	0.27	0.34	0.44	0.37	0.45	0.43	0.53	0.52	0.55	0.50	0.57	0.56	0.61	0.55
MgO	17.8	17.4	17.2	17.0	17.9	17.9	18.2	18.3	27.2	27.0	25.7	25.3	22.4	23.6	22.5	22.4
CaO	17.9	17.7	18.9	18.7	16.4	16.5	15.9	15.6	2.24	2.53	3.63	4.01	6.39	4.41	5.42	6.06
Total	99.6	100.5	99.8	99.5	99.3	99.8	100.6	100.8	100.5	100.2	99.0	98.9	99.8	100.4	101.3	100.6
Cations per 6 oxygen																
Si	1.955	1.934	1.955	1.953	1.965	1.958	1.940	1.934	1.981	1.982	1.968	1.959	1.962	1.976	1.951	1.976
Ti	0.007	0.014	0.007	0.010	0.007	0.009	0.011	0.013	0.002	0.002	0.002	0.002	0.016	0.014	0.024	0.013
Al	0.055	0.088	0.060	0.062	0.054	0.059	0.079	0.087	0.019	0.017	0.028	0.026	0.045	0.035	0.043	0.046
Cr	0.023	0.025	0.027	0.027	0.022	0.023	0.026	0.023	0.012	0.012	0.015	0.013	0.014	0.012	0.010	0.012
V	0.002	0.002	0.001	0.002	0.001	0.004	0.003	0.004	0.000	0.001	0.001	0.001	0.001	0.002	0.000	0.000
Fe	0.258	0.272	0.244	0.245	0.285	0.288	0.305	0.313	0.433	0.429	0.432	0.458	0.459	0.478	0.517	0.467
Mn	0.011	0.010	0.008	0.011	0.014	0.012	0.014	0.013	0.016	0.016	0.017	0.015	0.018	0.017	0.019	0.017
Mg	0.980	0.953	0.945	0.940	0.989	0.985	0.995	0.999	1.453	1.446	1.403	1.387	1.225	1.280	1.222	1.214
Ca	0.707	0.698	0.748	0.743	0.651	0.654	0.623	0.610	0.086	0.097	0.142	0.158	0.251	0.172	0.212	0.237
Sum	3.998	3.995	3.994	3.992	3.989	3.990	3.995	3.996	4.002	4.002	4.008	4.019	3.992	3.986	3.998	3.982
En	50.4	49.6	48.8	48.7	51.4	51.1	51.7	52.0	73.7	73.3	71.0	69.3	63.3	66.3	62.6	63.3
Wo	36.4	36.3	38.6	38.5	33.8	33.9	32.4	31.7	4.4	4.9	7.2	7.9	13.0	8.9	10.8	12.3
Fs	13.2	14.1	12.6	12.7	14.8	14.9	15.9	16.3	22.0	21.8	21.8	22.8	23.7	24.8	26.5	24.4

<sup>a</sup>Core.<sup>b</sup>Rim.

Endmembers of pyroxene in mol%. En: enstatite; Wo: wollastonite; Fs: ferrosilite. n.d.: below detection limit.

Table 5. Representative analyses of plagioclase and merrillite in GRV 99027, wt%.

	Plagioclase						Merrillite	
	1 <sup>a</sup>	2 <sup>a</sup>	3 <sup>b</sup>	4 <sup>c</sup>	5 <sup>b</sup>	6 <sup>c</sup>	7	8
SiO <sub>2</sub>	57.5	56.0	58.5	59.2	54.5	54.0		
TiO <sub>2</sub>	n.d.	n.d.	n.d.	n.d.	0.08	0.13		
Al <sub>2</sub> O <sub>3</sub>	26.7	26.9	25.7	25.3	27.7	27.5		
Cr <sub>2</sub> O <sub>3</sub>	n.d.	n.d.	n.d.	n.d.	n.d.	0.13		
FeO	0.37	0.44	0.32	0.33	0.59	0.90	1.57	2.04
MgO	0.14	0.33	0.09	0.12	0.16	0.30	3.62	3.81
MnO							n.d.	0.06
CaO	9.87	11.0	9.93	8.91	11.6	11.9	45.7	45.9
Na <sub>2</sub> O	6.24	5.43	6.36	6.71	5.08	5.03	0.72	0.52
K <sub>2</sub> O	0.21	0.14	0.18	0.24	0.07	0.08	n.d.	n.d.
P <sub>2</sub> O <sub>5</sub>							45.7	45.5
Cl							n.d.	n.d.
Total	101.0	100.2	101.1	100.8	99.7	100.0	97.4	97.9
Cations per formula unit								
Si	2.564	2.522	2.604	2.636	2.474	2.457		
Ti	0.000	0.000	0.000	0.000	0.003	0.004		
Al	1.401	1.430	1.347	1.325	1.482	1.474		
Cr	0.000	0.000	0.000	0.000	0.000	0.005		
Fe	0.014	0.017	0.012	0.012	0.022	0.034	0.238	0.315
Mg	0.009	0.022	0.006	0.008	0.011	0.020	0.987	1.036
Mn							0.007	0.007
Ca	0.471	0.532	0.474	0.425	0.563	0.580	8.953	8.974
Na	0.539	0.474	0.549	0.579	0.447	0.443	0.252	0.182
K	0.012	0.008	0.010	0.014	0.004	0.005	0.000	0.000
P							7.070	7.028
Cl							0.000	0.000
Sum	5.011	5.005	5.002	4.998	5.006	5.022	17.507	17.542
An	46.1	52.5	45.9	41.7	55.5	56.4		
Or	1.2	0.8	1.0	1.4	0.4	0.5		

<sup>a</sup>In contact with void.<sup>b</sup>Core.<sup>c</sup>Rim.

Endmembers of plagioclase (in mol%). An: anorthite; Or: orthoclase. n.d.: below detection limit; blank: not analyzed.

chadacrysts suggest partial absorption by melt, consistent with a cumulate origin of the mineral. The size distribution pattern of olivine with a turndown feature at the smallest size fraction (Fig. 3b) is probably due to the absorption. Although annealing processes or continuous growth of olivine without nucleation can also result in a similar size distribution pattern (Lentz and McSween 2000), we found no supporting petrographic or mineral chemical evidence for these scenarios in our section. The abundances of olivine in both poikilitic and interstitial lithologies are nearly the same (Table 1), suggesting that no additional olivine crystallized from the intercumulus melt or accumulated from the magma chamber after formation of the pigeonite oikocryst. The olivine chadacrysts are isolated in pigeonite, protected from reacting with the interstitial melt. In contrast, other grains in the interstitial lithology probably equilibrated with the intercumulus melt and became more FeO-enriched with higher contents of Al<sub>2</sub>O<sub>3</sub>, TiO<sub>2</sub>, and Cr<sub>2</sub>O<sub>3</sub>. Besides olivine, chromite is another cumulus crystal. The occurrence of

chromite as inclusions in olivine indicates its earlier formation than the host phase.

Pigeonite mainly crystallized from the intercumulus melt and thus is not of cumulative origin, as are olivine and chromite. The identical orientation patterns of olivine in both poikilitic and interstitial lithologies (Fig. 3a) argue for in situ growth of the pigeonite oikocryst from the intercumulus melt, because if the oikocryst had accumulated from a magma chamber, the orientation pattern and abundance of olivine in the poikilitic lithology would have been different from those in the interstitial region. After pigeonite, augite crystallized from the melt, partly precipitating as rims on the pigeonite oikocryst. Plagioclase and minor phases, such as merrillite, Ti-rich chromite, and ilmenite are the last minerals to crystallize from the residual melt. The increase of Ti concentration in the residual melt is also indicated by the zoning profiles of chromite, with TiO<sub>2</sub> contents up from 0.9 wt% in cores to 11.1 wt% in rims (Fig. 10b).

We computed crystallization sequences of magmas with

Table 6. Representative analyses of chromite and ilmenite in GRV 99027, wt%.

	Interstitial				Poikilitic						Ilmenite		
	1 <sup>a</sup>	2 <sup>b</sup>	3 <sup>a</sup>	4 <sup>b</sup>	5 <sup>a</sup>	6 <sup>b</sup>	7 <sup>a</sup>	8 <sup>b</sup>	9	10	11 <sup>a</sup>	12 <sup>b</sup>	13
MgO	4.69	6.07	4.32	5.44	6.60	6.75	6.71	6.98	4.96	5.24	6.39	6.42	6.80
Cr <sub>2</sub> O <sub>3</sub>	39.9	38.3	32.0	33.1	58.8	57.1	61.5	59.5	54.7	52.5	0.61	0.59	0.82
Al <sub>2</sub> O <sub>3</sub>	7.05	7.42	6.48	6.83	7.44	8.23	5.46	5.99	9.71	11.2	0.11	0.11	0.19
MnO	0.62	0.45	0.52	0.47	0.37	0.39	0.37	0.33	0.49	0.40	0.64	0.63	0.65
TiO <sub>2</sub>	9.40	9.67	12.4	13.1	1.04	1.25	0.82	0.94	1.07	1.11	54.6	54.6	54.6
FeO	37.4	35.2	41.6	38.6	25.0	24.7	25.0	24.7	28.2	28.3	36.6	36.4	35.9
V <sub>2</sub> O <sub>3</sub>	0.47	0.58	0.57	0.54	0.45	0.46	0.39	0.47	0.47	0.41	0.02	n.d.	n.d.
NiO	n.d.	0.13	0.08	0.10	n.d.	n.d.	n.d.	0.08	n.d.	n.d.	n.d.	n.d.	n.d.
Total	99.5	97.8	98.0	98.2	99.7	98.9	100.3	99.0	99.6	99.2	99.0	98.8	99.1
Cations per formula													
Mg	0.244	0.317	0.229	0.285	0.337	0.346	0.344	0.360	0.254	0.267	0.231	0.233	0.245
Cr	1.099	1.060	0.900	0.919	1.595	1.553	1.673	1.630	1.486	1.419	0.012	0.011	0.016
Al	0.289	0.306	0.271	0.283	0.301	0.334	0.222	0.245	0.393	0.452	0.003	0.003	0.005
Mn	0.019	0.013	0.016	0.014	0.011	0.011	0.011	0.010	0.014	0.012	0.014	0.013	0.014
Ti	0.247	0.255	0.332	0.345	0.027	0.033	0.021	0.025	0.028	0.029	0.995	0.996	0.992
Fe	1.088	1.030	1.235	1.133	0.717	0.710	0.719	0.715	0.811	0.811	0.741	0.740	0.726
V	0.013	0.016	0.017	0.015	0.012	0.013	0.011	0.013	0.013	0.011	0.001	0.000	0.000
Ni	0.001	0.004	0.002	0.003	0.001	0.000	0.000	0.002	0.001	0.000	0.001	0.001	0.001
Sum	3.000	2.999	3.000	2.996	3.000	3.000	3.000	3.000	3.000	3.000	1.997	1.996	1.998
Fe <sup>3+</sup> /Fe	9.7	10.5	12.3	8.4	5.2	4.9	7.4	8.9	6.5	7.5			
Chm	55.0	53.0	45.0	45.9	79.7	77.7	83.6	81.5	74.3	71.0			
Sp	15.1	16.1	14.4	14.9	15.6	17.3	11.6	12.9	20.3	23.1			
Mt	5.3	5.4	7.6	4.7	1.9	1.7	2.6	3.2	2.6	3.0			
Usp	24.7	25.5	33.2	34.5	2.7	3.3	2.1	2.5	2.8	2.9			

<sup>a</sup>Core.<sup>b</sup>Rim.

9–10: included in olivine; 13: small grain in contact with chromite. Endmembers of chromite in mol%. Chm: chromite; Sp: spinel; Mt: magnetite; Usp: ulvöspinel; Fe<sup>3+</sup> calculated based on stoichiometry of chromite. n.d.: below detection limit.



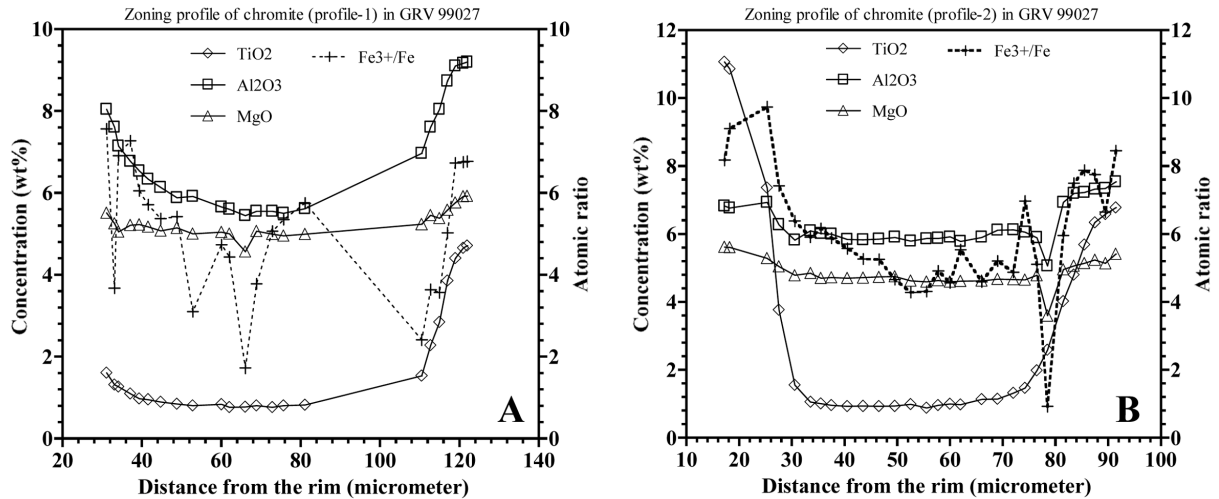


Fig. 10. EPMA profiles of chromite in the poikilitic lithology (a) and in the interstitial (b), both showing increase of TiO<sub>2</sub> and Al<sub>2</sub>O<sub>3</sub> contents toward the rim. Fe<sup>3+</sup> is calculated based on stoichiometry of chromite.

the bulk composition of GRV 99027 and the inferred intercumulus melt (Table 2; see also the Parent Magma section below) using the MELTS program (Ghiorso and Sack 1995; Asimow and Ghiorso 1998), under conditions of 1 bar pressure and an average oxygen fugacity of  $\log \Delta f_{O_2}(\text{QFM}) = -2.0$  (relative to the quartz-fayalite-magnetite buffer; see also the Formation Temperature and Oxygen Fugacity section below). The computed result of the bulk GRV 99027 shows a continuous crystallization of olivine, with the mass fraction of olivine increasing quickly at the beginning and then being nearly constant at 1200 °C (Fig. 13a). The continuous precipitation of olivine along with low-Ca pyroxene is different from our observations, e.g., the identical patterns of orientation and size distribution and the similar abundances of olivine in the two lithologies. This scenario does not predict the rounded shape of olivine, which is a result of absorption by melt. In contrast, our petrographic observations are consistent with the computed crystallization of the intercumulus melt, which shows a slight decrease of olivine abundance during early crystallization of low-Ca pyroxene (Fig. 13b).

#### Parent Magma

The bulk composition of GRV 99027 is not the same as its parent magma, since the rock is a cumulate. As discussed above, the computed crystallization of the bulk GRV 99027 is inconsistent with the observed petrographic textures. Instead, the intercumulus melt probably represents the parent magma of GRV 99027, which we calculated from the modal composition and the average mineral chemistries with an assumption of cumulus olivine and chromite (Table 2). The intercumulus melt contains more SiO<sub>2</sub> (54.5 wt%), but less Al<sub>2</sub>O<sub>3</sub> (2.65) and FeO (13.0 wt%) than those of ALH 77005 (SiO<sub>2</sub> 48.3 wt%, Al<sub>2</sub>O<sub>3</sub> 5.76 wt%, FeO 15.6 wt%) (McSween et al. 1988). REEs of the intercumulus melt were calculated in

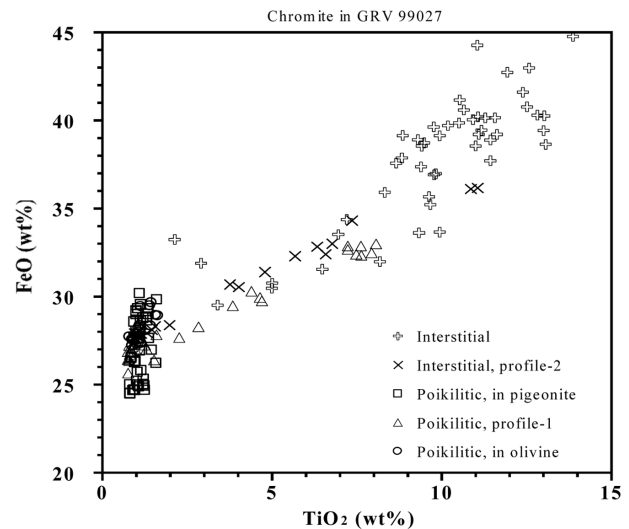


Fig. 11. FeO-TiO<sub>2</sub> plot of chromite shows different trends between both occurrences. Grains in the interstitial lithology contain higher TiO<sub>2</sub> and FeO than those in the poikilitic.

the same way. The inferred REE pattern is identical to that of the bulk GRV 99027, but with slightly higher abundances than the latter (Fig. 12d).

We have also calculated REE abundances of melts in equilibrium with the minerals, using the mineral/melt partition coefficients reported for basaltic shergottites by Norman (1999). Analysis Pig-7 was measured on the core of the oikocrystic pigeonite; it thus represents the composition of the first pyroxene to crystallize from the parent magma. The calculated REE pattern (especially HREE) of the magma is close to that of the intercumulus melt (Fig. 14). The melt in equilibrium with the average augite has the highest REE abundance, consistent with late precipitation of the mineral. The variation of REE of the magma during crystallization is

Table 7. Representative SIMS analyses of minerals in GRV 99027, ppm.

	Ol-2	Pig-5	Pig-6	Aug-4P	Aug-5r	Pl-2	P-1	MI-1
Rb	2.60±0.0490	6.79±0.11	9.37±0.43	9.66±0.23	6.51±0.18	3.47±0.17	3.6±0.3	14.7±0.4
Sr	0.030±0.0030	0.755±0.019	0.305±0.044	2.37±0.06	3.91±0.08	136±0.6	150±0.9	51.5±0.4
Ba	0.008±0.0010	0.208±0.011	0.110±0.016	0.45±0.03	0.51±0.03	23.5±0.3	11.4±0.3	19.7±0.3
Nb	0.0010±0.0005	0.023±0.002	0.007±0.004	0.08±0.01	0.06±0.01	0.019±0.004	0.38±0.03	1.29±0.04
Zr	0.041±0.0050	3.00±0.05	0.334±0.065	1.63±0.07	6.62±0.13	0.950±0.066	43.0±0.7	95.9±0.8
Sc	3.61±0.0190	49.7±0.1	36.7±0.3	81.3±0.2	106.3±0.22	19.5±0.1	62.3±0.3	78.1±0.3
Y	0.072±0.0040	5.73±0.05	0.645±0.055	5.16±0.08	11.6±0.11	0.180±0.018	486±1.5	39.8±0.3
La	0.0010±0.0005	0.047±0.003	0.017±0.005	0.11±0.01	0.14±0.01	0.254±0.017	36.8±0.4	1.66±0.05
Ce	0.0025±0.0005	0.093±0.005	0.017±0.005	0.16±0.01	0.37±0.02	0.304±0.019	82.7±0.7	3.34±0.08
Pr	0.0005±0.0005	0.026±0.002		0.028±0.004	0.089±0.007	0.043±0.007	12.4±0.2	0.49±0.03
Nd	0.0025±0.0005	0.199±0.007	0.020±0.007	0.27±0.02	0.62±0.02	0.191±0.016	81.7±0.7	3.14±0.07
Sm	0.0015±0.0005	0.222±0.010	0.004±0.004	0.24±0.02	0.70±0.03	0.052±0.013	49.7±0.7	1.97±0.08
Eu	0.0005±0.0000	0.076±0.004	0.008±0.004	0.10±0.01	0.27±0.01	1.015±0.034	20.0±0.3	1.23±0.05
Gd	0.0035±0.0010	0.514±0.026	0.049±0.013	0.56±0.04	1.51±0.06	0.072±0.015	72.4±1.2	4.26±0.14
Tb	0.0005±0.0005	0.128±0.006	0.022±0.005	0.11±0.01	0.35±0.02	0.005±0.003	13.9±0.3	0.96±0.04
Dy	0.0095±0.0005	0.975±0.017	0.116±0.012	0.94±0.03	2.21±0.04	0.029±0.006	97.1±0.8	6.44±0.10
Ho	0.0030±0.0005	0.210±0.007	0.017±0.005	0.21±0.01	0.48±0.02	0.010±0.003	19.2±0.3	1.54±0.05
Er	0.0105±0.0005	0.614±0.015	0.089±0.013	0.53±0.02	1.27±0.04	0.024±0.007	47.2±0.6	4.17±0.09
Tm	0.0020±0.0005	0.089±0.005	0.015±0.005	0.09±0.01	0.16±0.01	0.015±0.008	5.6±0.2	0.65±0.03
Yb	0.0135±0.0010	0.677±0.014	0.082±0.011	0.55±0.02	1.23±0.03	0.009±0.005	37.1±0.6	4.81±0.10
Lu	0.0030±0.0005	0.094±0.006	0.022±0.006	0.07±0.01	0.15±0.01		4.4±0.2	0.62±0.04

Note: The analysis labels are the same used in Fig. 12. Analysis errors are given as  $\pm 1\sigma$ , on counting statistics.

Abbreviations: Ol: olivine; Pig: pigeonite; Aug: augite; Pl: plagioclase; P: merrillite; MI: melt inclusion.

confirmed by the results determined from mass balance and the computed crystallization sequence of the intercumulus melt (Fig. 14). The liquid that equilibrated with olivine shows a distinct REE pattern from others, probably suggesting a different magma source. Because of the extremely low REEs in olivine, however, large uncertainties in REE partition coefficients of olivine/melt can be an alternative reason.

The occurrence of magmatic inclusions in olivine suggests an early capture by the host mineral at the beginning of crystallization of GRV 99027. However, compositions of the inclusions have been highly modified by growth of olivine. Except for the elongated and crystallized inclusion in the largest olivine chadacryst, the broad beam analyses of other magmatic inclusions have significantly higher  $\text{SiO}_2$  (60.4–62.4 wt%) and lower  $\text{MgO}$  (2.10–2.77 wt%) (Table 2) than those of their counterparts in ALHA77005 (Table 3, Ikeda 1998). The highly evolved compositions of the magmatic inclusions are also confirmed by their significantly higher REE abundances than those of the bulk and intercumulus melts (Fig. 12d), which may be due to the growth of olivine on the walls of the magmatic inclusions.

#### Closed or Open System

Except for the cumulus olivine and chromite, GRV 99027 probably crystallized from a closed system with a composition similar to that of the inferred intercumulus melt. The zoning profiles of large chromite grains with both  $\text{Al}_2\text{O}_3$  and  $\text{TiO}_2$  increasing from core to rim (Fig. 10) reflect enrichment of these components in residual liquids during crystallization of a closed system. As discussed above, the observed mineral assemblage and textural relationship of

GRV 99027 are consistent with equilibrium crystallization of the intercumulus melt computed using the MELTS program. Furthermore, we determined REE patterns of the related residual liquids during such a crystallization process based on mass balance, and the results overlap with those determined by mineral/melt partitioning (Fig. 14). These lines of evidence support crystallization in a closed system.

On the other hand, the chromite inclusions in olivine contain higher  $\text{Al}_2\text{O}_3$  than those in the oikocrystic pigeonite (Fig. 9). The two occurrences of chromite have low and nearly identical Ti content. The higher  $\text{Al}_2\text{O}_3$  of chromite in olivine could not be expected from crystallization in a closed system, because precipitation of  $\text{Al}_2\text{O}_3$ -poor olivine would increase  $\text{Al}_2\text{O}_3$  content of the melt, and thus that of chromite in pyroxene. The low  $\text{Al}_2\text{O}_3$  content of chromite in the pigeonite indicates a decrease of  $\text{Al}_2\text{O}_3$  concentration in the magma reservoir after precipitation of olivine. A possible scenario is that the original magma was diluted by another melt with lower concentration of  $\text{Al}_2\text{O}_3$ , which was also suggested in a previous report for ALH 77005 (Ikeda 1994). Another hint for an early mixing of the parent magma is the calculated REE pattern of the melt equilibrated with olivine, which is significantly different from that of the inferred intercumulus melt (Fig. 14). However, as mentioned above, large uncertainties in REE partition coefficients of olivine/melt cannot be excluded.

#### Formation Temperature and Oxygen Fugacity

We determined formation temperatures of GRV 99027 using various geothermometers (Table 8). Subsolvus temperatures of coexisting pigeonite and augite vary within a

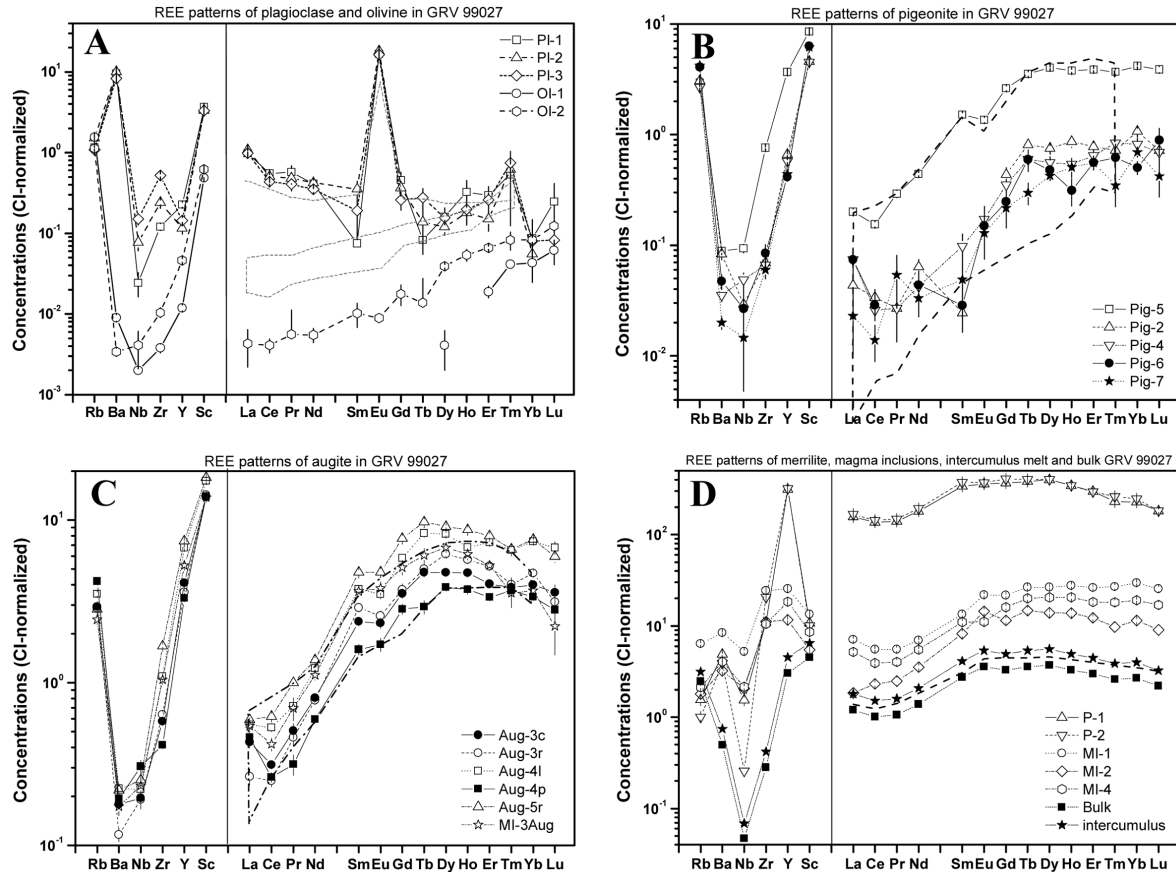


Fig. 12. REE patterns of minerals in GRV 99027. a) Olivine and plagioclase. b) Pigeonite. c) Augite. d) Merrillite, magmatic inclusions, and the bulk and intercumulus melts. The ranges of ALHA77005 (dotted lines) are shown for comparison, with in situ analyses from Lundberg et al. (1990) and bulk data from Shih et al. (1982). Error bars are  $1\sigma$ .

narrow range of 1100–1200 °C, according to the two-pyroxene thermometer (Lindsley and Andersen 1983). No significant difference was found between the formation temperatures of poikilitic and interstitial lithologies, which is consistent with simultaneous formation of the two lithologies as discussed above. Ca exchange between olivine and augite is sensitive to temperature and pressure variations (Kohler and Brey 1990). Assuming a shallow burial depth ( $\sim 0$  kbar), closure temperatures of the mineral pairs in the interstitial lithology are calculated to be 1170–1210 °C, consistent with the results of the two-pyroxene thermometer. Olivine in the poikilitic lithology is isolated in pigeonite; hence the olivine-augite geothermometer cannot be applied.

Oxygen fugacity of the parent magma of GRV 99027 can be determined using an olivine-orthopyroxene-chromite barometer (Table 8). We calculated the equilibrium temperatures of the assemblages based on  $Mg^{2+}$  and  $Fe^{2+}$  diffusion between olivine and chromite (Sack and Ghiorso 1991), and computed the activity of magnetite component in chromite using MELTS. We assume that GRV 99027 crystallized near the surface of Mars ( $\sim 0$  kbar). This assumption does not significantly change the result, because

the oxygen fugacity is insensitive to pressure (Wood 1991). The determined oxygen fugacities in log units are from  $-1.5$  to  $-2.5$  with an average of  $-2.0 \pm 0.4$  relative to the quartz-fayalite-magnetite (QFM) buffer, and the correlated temperatures are in a range of 960–1360 °C. Such oxygen fugacities are close to the middle of the previously documented range for basaltic shergottites (Fig. 15).

We also determined both equilibrium temperature and oxygen fugacity of GRV 99027 (Table 8), using the ilmenite-chromite geothermometer and oxygen barometer (Ghiorso and Sack 1991). The analyses of ilmenite are not corrected for existence of chromite, because large grains of ilmenite in GRV 99027 contain no chromite inclusions and are homogeneous in their backscattered electron images. The calculation shows wide ranges of temperature (1130–480 °C) and oxygen fugacity ( $\Delta \log_{10} f_{O_2}(QFM)$ :  $-1.0 \sim -7.0$ ), and the maximum temperature (1130 °C) and the correlated oxygen fugacity ( $-1.0$ ) are within the range determined by the olivine-orthopyroxene-chromite assemblages (Fig. 15). The oxygen fugacity is correlated with the temperature, suggesting the subsolidus equilibration was approached at much lower temperature for chromite-ilmenite than for

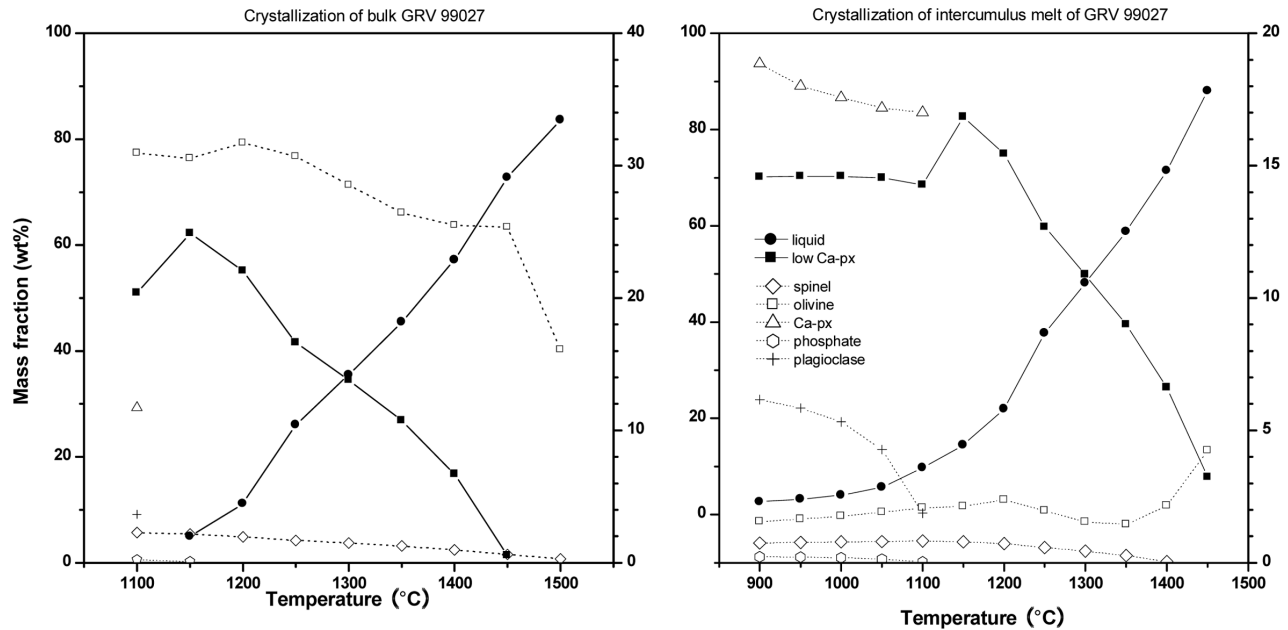


Fig. 13. The computed crystallization of melts with the bulk composition of GRV 99027 (a) and that of the inferred intercumulus melt (b). Mass fractions of low-Ca pyroxene (px) and liquid are plotted relative to the left y-axis, and others relative to the right y-axis. As temperature decreases, mass fraction of olivine increases continuously from the bulk meteorite melt, in comparison with the decreasing trend at the earliest stage of crystallization of the intercumulus melt.

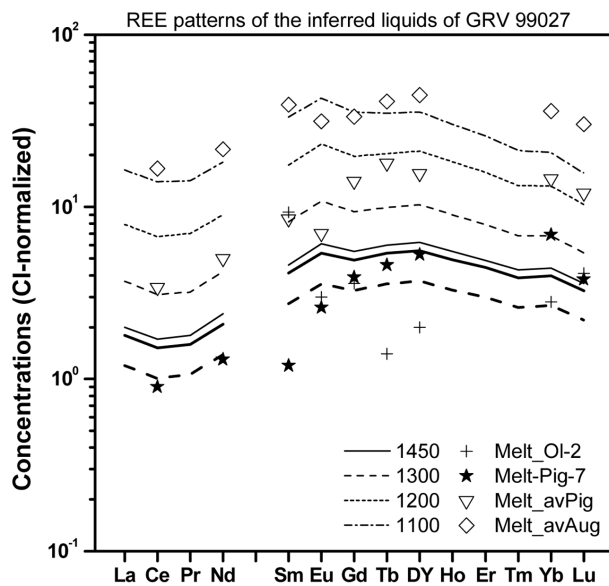


Fig. 14. REE patterns of the residual melts calculated from 1450 to 1100 °C, in comparison with the liquids in equilibrium with the minerals. The bulk melt (heavy line) and inferred intercumulus melt (heavy dashed line) of GRV 99027 are shown too. Note similarity of HREE between the intercumulus melt with the liquid in equilibrium with the core of the oikocrystic pigeonite. Liquid in equilibrium with average augite has the highest REE and similar to that of the last residual melt at 1100 °C. Olivine shows significant deviation from the possible parent melt. The REE partition factors after Norman (1999).

silicates. Similar subsolidus equilibration between ilmenite-chromite under reducing conditions has been reported (Ghosal et al. 1998; Hale and McSweeney 1999; Xirouchakis et al. 2002). However, GRV 99027 appears to have recorded the lowest subsolidus temperatures of any shergottites, suggesting a slower cooling history than other specimens in this Martian meteorite subgroup.

#### Correlation of $fO_2$ with REE Ratios

The Eu distribution between Ca-pyroxene and magma of basaltic shergottites correlates with oxygen fugacity, and such a correlation is used as an oxygen barometer (Wadhwa 2001). Assuming the intercumulus melt as the parent magma of GRV 99027, Eu and Gd distribution ratios between augite and the magma,  $D_{Eu}/D_{Gd}$ , is  $0.57 \pm 0.04$ , and the result plots on the trend of basaltic shergottites on the  $D_{Eu}/D_{Gd}$  ratio versus  $fO_2$  diagram (Fig. 16a). The  $D_{Eu}/D_{Gd}$  ratio of GRV 99027 is slightly higher than those of the other lherzolites (Y-793605: 0.49; LEW 88516: 0.35–0.46), which are estimated from the reported SIMS data of augite (Harvey et al. 1993; Wadhwa et al. 1999) and the INAA data of the bulk meteorites with Gd replaced by Tb (Dreibus et al. 1992; Warren and Kallemeyn 1997). Although these lherzolites are cumulates, REE patterns of their parent magmas should be similar to those of the bulk meteorites except for different absolute values, because the cumulus olivine and chromite are REE-poor. The smaller negative Eu-depletion of augite in GRV 99027 (CI-normalized Eu/Gd:  $0.65 \pm 0.06$ ) than other lherzolites (0.39–0.56) is consistent with the above estimation.



Table 8. Representative temperatures and oxygen fugacities of GRV 99027.

	Augite-olivine			Chromite-olivine-pigeonite			Chromite-ilmenite		
SiO <sub>2</sub>	52.1	37.9	0.09	38.2	54.5	n.d.	n.d.	n.d.	n.d.
TiO <sub>2</sub>	0.55	0.04	1.14	n.d.	0.09	13.0	53.5	11.9	53.2
Al <sub>2</sub> O <sub>3</sub>	2.44	0.00	7.61	n.d.	0.68	5.65	0.27	6.15	0.21
Cr <sub>2</sub> O <sub>3</sub>	0.97	0.06	57.5	0.08	0.74	32.1	0.65	31.8	0.58
V <sub>2</sub> O <sub>3</sub>	0.08	n.d.	0.70	n.d.	0.05	0.59	0.06	0.53	0.01
FeO	9.26	27.6	28.6	24.1	14.7	39.4	35.6	42.7	35.9
MnO	0.38	0.58	0.06	0.57	0.52	0.49	0.54	0.50	0.68
MgO	16.9	36.1	5.69	38.8	24.9	5.63	7.48	4.18	6.48
CaO	17.58	0.22	n.d.	0.10	4.49	0.09	0.68	n.d.	0.06
Total	100.25	102.59	101.41	101.89	100.60	96.93	98.75	97.77	97.20
Si	1.923	0.987	0.003	0.985	1.972	0.000	0.000	0.000	0.000
Ti	0.015	0.001	0.029	0.000	0.003	0.349	0.966	0.320	0.987
Al	0.106	0.000	0.304	0.001	0.029	0.237	0.007	0.259	0.006
Cr	0.028	0.001	1.543	0.002	0.021	0.904	0.013	0.895	0.011
V	0.002		0.019		0.002	0.017	0.001	0.015	0.000
Fe	0.286	0.601	0.811	0.519	0.444	1.175	0.715	1.274	0.741
Mn	0.012	0.013	0.002	0.012	0.016	0.015	0.011	0.015	0.014
Mg	0.927	1.402	0.288	1.492	1.340	0.299	0.268	0.222	0.238
Ca	0.695	0.006	0.001	0.003	0.174	0.003	0.017	0.000	0.001
T °C	1163 <sup>a</sup>			1085 <sup>b</sup>			1130 <sup>c</sup>		
<i>f</i> O <sub>2</sub> <sup>c</sup>				-1.944 <sup>d</sup>			-1.05 <sup>c</sup>		
							480 <sup>c</sup>		
							-6.97 <sup>c</sup>		

<sup>a</sup>Calculation is after Kohler and Brey (1990).<sup>b</sup>Calculation is after Sack and Ghiorso (1991).<sup>c</sup>Calculation is after Ghiorso and Sack (1991).<sup>d</sup>Calculation is after Wood (1991).<sup>e</sup>In log unit and relative to QFM buffer. Activity of magnetite component in chromite was determined using MELT program.

The CI-normalized La/Yb ratio of bulk GRV 99027 (0.46) also plots in the middle of basaltic shergottites on the diagram of La/Yb versus *f*O<sub>2</sub>, close to the values of ALHA77005 (Fig. 16b). Similarly, the ratio of GRV 99027 is slightly higher than those of Y-793605 (0.36) and LEW 88516 (0.35), and close to that of ALH 77005 (0.43). The low oxygen fugacity and LREE-depletion of the parent magma of GRV 99027 suggests a relatively low degree of contamination of this magma by Martian crust or other enriched sources.

### Genetic Relationship with other Lherzolitic Shergottites

#### Distinct Thermal Metamorphism

Maskelynite in GRV 99027 shows almost full recrystallization compared to ALHA77005, Y-793605 and LEW 88516. This suggests a high degree of post-impact thermal metamorphism for GRV 99027 relative to other lherzolitic shergottites. All plagioclase in GRV 99027 shows undulose extinction in polarized light, indicating a crystalline phase instead of diaplectic glass. The plagioclase should form through recrystallization of maskelynite during a post-shock thermal metamorphism. In contrast, plagioclase in other lherzolitic shergottites occurs as maskelynite. Partial recrystallization of maskelynite along grain boundaries was reported only in ALHA77005 (Ikeda 1994; Treiman et al. 1994). The other new lherzolitic shergottite, GRV 020090,

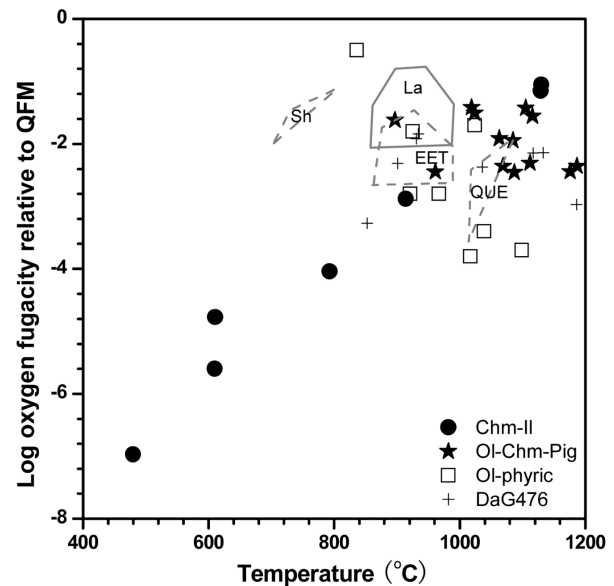


Fig. 15. O<sub>2</sub> versus temperatures of GRV 99027. The oxygen fugacity and related temperature of GRV 99027 are calculated using the olivine-chromite-pigeonite (Ol-Chm-OPx) barometer. The chromite-ilmenite (chm-Il) barometer shows wide ranges of oxygen fugacity and temperature towards highly reducing conditions at low temperatures. Ranges of basaltic shergottites with abbreviations (Xirouchakis et al. 2002) and DaG 476 (Herd et al. 2002) and olivine-phyric shergottites (Ol-phyric) (Goodrich et al. 2003a) shown for comparison.

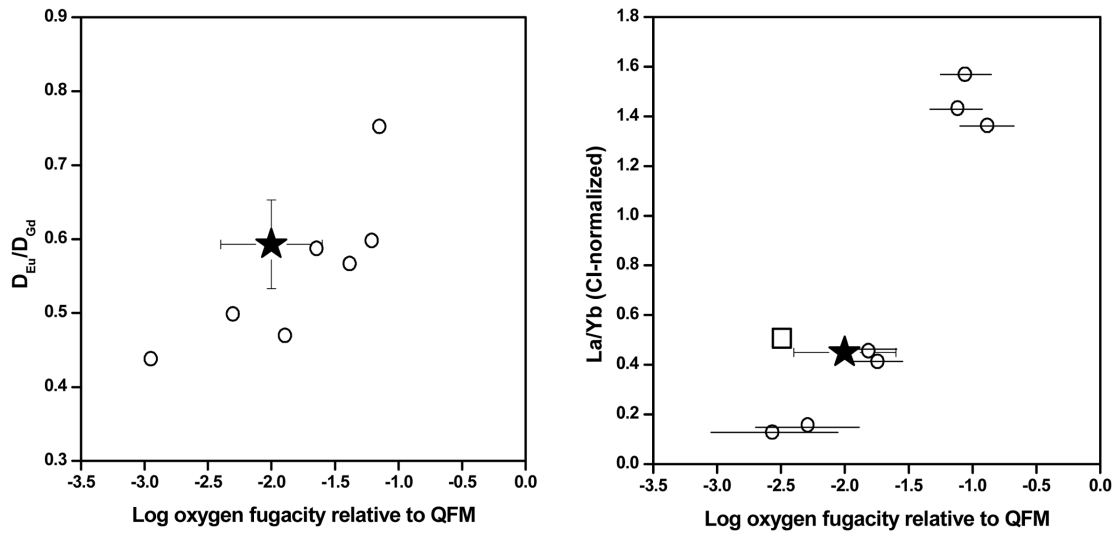


Fig. 16. Correlation of oxygen fugacity with REE ratios of GRV 9907 (filled star). a)  $D_{Eu}/D_{Gd} - O_2$ . b) CI-normalized  $La/Yb - O_2$ . Data of basaltic shergottites (open circles) from Herd et al. (2002) and ALHA77005 (open square) from Warren and Bridges (2005).

shows clear glass without any recrystallization (Miao et al. 2004).

The high degree of thermal metamorphism of GRV 99027 is supported by its very homogeneous mineral chemistry. In spite of variation among grains, our EPMA profiles and analyses of the cores and rims of large grains of olivine, pyroxenes and plagioclase show no significant zoning features. This is consistent with the previous report by Hsu et al. (2004). In contrast, compositional zonings of silicates have been reported in other lherzolitic shergottites, accordingly suggesting a trend of increasing degree of re-equilibration from Y-793605 to LEW 88516 to ALHA77005 (Mikouchi and Miyamoto 2000). In addition, as discussed above, the chromite-ilmenite geothermometer of GRV 99027 demonstrates very low subsolidus equilibrium temperatures of the oxides, consistent with a high degree of thermal metamorphism.

#### *Launch Pairing or Homogeneous Martian Mantle?*

As discussed above, GRV 99027 experienced distinct thermal metamorphism than other lherzolitic shergottites. Furthermore, GRV 99027 contains lower olivine (32.1 vol%) than ALHA77005, Y-793605, and LEW 88516 (40–60 vol%, Delaney 1992; Treiman et al. 1994; Gleason 1997; Ikeda 1997; Mikouchi and Miyamoto 1997). The lower abundance of olivine is probably intrinsic instead of a sampling bias, because both the poikilitic and interstitial lithologies of GRV 99027 have nearly identical abundances of olivine (Table 1). Plagioclase is also less abundant in GRV 99027 than in other lherzolites. This difference could be related to heterogeneity of the sample, because plagioclase is confined to the interstitial lithology. However, the lack of negative Eu-anomaly in merrillite (Fig. 12d) suggests an intrinsic low abundance of plagioclase in GRV 99027. In contrast, the

pronounced negative Eu-anomalies of merrillite in other lherzolites suggest precipitation of abundant plagioclase, the most Eu-rich mineral in these meteorites. Another distinguishing feature is the absence of magmatic inclusions in the pyroxene oikocrysts in GRV 99027, which are common in other lherzolites (e.g., Ikeda 1998; Mikouchi and Miyamoto 2000) except for GRV 020090. The above differences demonstrate that GRV 99027 is not “fall pairing” with other lherzolitic shergottites, which is consistent with the long distances between their find locations.

Other than the above differences, GRV 99027 shows similar petrographic, mineral chemical and geochemical features with other lherzolitic shergottites, especially with ALHA77005, consistent with the previous report (Hsu et al. 2004). The similarities among lherzolitic shergottites are remarkable, in comparison with the wide variations of basaltic shergottites. All lherzolitic shergottites, including GRV 99027, have two lithologies. The poikilitic lithology consists of pigeonite oikocrysts with inclusions of rounded olivine and euhedral chromite, whereas the interstitial part is composed of euhedral to subhedral pigeonite, augite, and plagioclase with minor merrillite, chromite, ilmenite, and sulfides. Pyroxenes, olivine, and chromite are systematically more FeO-rich in the interstitial lithology than in the poikilitic one. In addition, oxygen isotopic compositions of GRV 99027 (Lin et al. 2003) and other lherzolites (Clayton and Mayeda 1996) fall within a narrow range relative to basaltic shergottites. REE patterns of the major constituents in GRV 99027 are similar to those of the counterparts in ALHA77005, except for lower REE abundance of olivine in the former than in the latter (Fig. 12a). The calculated bulk REE pattern of GRV 99027 shows a hump-like shape, and is nearly identical to that of ALHA77005 (Fig. 12d).

The discovery of GRV 99027 confirms similarity among

lherzolitic shergottites. One possibility is that these lherzolites represent a “launch pairing,” i.e., they were all ejected from the same igneous unit on Mars by the same impact event. This is supported by the overlapping ejection ages of LEW 888516, Y-793605 (Nyquist et al. 2001), and ALH 77005 (Eugster et al. 2002). The observed differences in thermal metamorphism and modal composition can be related to petrological variations within the same, relatively extensive igneous unit on Mars. The diversity observed among the lherzolitic shergottites is even less than launch paired lunar meteorites (Jolliff et al. 2004; Korotev et al. 2004), although the reverse might be expected because the ejection craters on Mars should be significantly larger than the counterparts on Moon based on computer simulations of launching meteorites from both objects (Head et al. 2002; Head 2003) and the observations of shock effects (Beck et al. 2005).

However, it is prudent to consider the alternative scenario in which the similarity of lherzolitic shergottites results from a relatively homogeneous upper mantle of Mars, if GRV 99027 and other lherzolitic shergottites sampled distinct igneous units on Mars, and were delivered to the Earth by different launch events. A previous study reported that ALHA77005 was launched about 1 Ma earlier than LEW 88516 and Y-793605 (Nyquist et al. 2001). In addition, ALHA77005 has the initial  $^{87}\text{Sr}/^{86}\text{Sr}$  and  $\epsilon^{143}\text{Nd}/^{144}\text{Nd}$  ratios distinguishable from those of LEW 88516, arguing for their distinct sources (Borg et al. 2002). However, determination of various event ages, including crystallization, major impact and launch of GRV 99027, is required to clarify whether or not this new Martian lherzolite is launch paired with the others.

## CONCLUSIONS

Textural relationships and REE distributions in GRV 99027 suggest equilibrium crystallization of a closed system after initial accumulation of chromite and olivine. The inferred mineral sequence is chromite, olivine, pigeonite, augite, plagioclase and assemblages of Ti-rich chromite, ilmenite and merrillite. The subsolidus temperatures of pyroxenes and olivine are  $\sim 1100\text{--}1210^\circ\text{C}$ , based on the two-pyroxene thermometer and Ca partitioning between olivine and augite. Oxygen fugacity of the magma is  $2.0 \pm 0.4$  log unit below QFM at  $960\text{--}1360^\circ\text{C}$ , using the olivine-orthopyroxene-chromite barometer. However, subsolidus equilibrium between chromite and ilmenite extended down to much lower temperatures ( $480^\circ\text{C}$ ) and oxygen fugacities (7.0 log unit below QFM). Such low subsolidus equilibrium temperatures suggest a slow cooling history of GRV 99027. This is consistent with the very homogeneous mineral chemistry and full re-crystallization of maskelynite in GRV 99027, a distinguishing feature of this sample from other lherzolitic shergottites.

Consistency of the textural observations, the computed crystallization sequence of the intercumulus liquid, and REE

partitioning of minerals suggests that the intercumulus liquid represents the parental magma composition of GRV 99027. The inferred parent magma contains higher  $\text{SiO}_2$ , but lower  $\text{Al}_2\text{O}_3$  and FeO than calculated parent melts for ALHA77005, Y-793605, and LEW 88516. The parent magma is LREE-depleted without a Eu anomaly. In addition, the Eu partition between augite and the parent magma is correlated with oxygen fugacity, lying within the trend of basaltic shergottites (Wadhwa 2001). The above observations suggest a low degree of contamination of the magma source of GRV 99027 by the crust or other evolved sources of Mars.

The discovery of GRV 99027 extends similarity of lherzolitic shergottites. One possibility is that all these samples are launch paired, i.e., these lherzolitic shergottites are fragments from various locations in the same igneous unit on Mars by a single impact event. Another scenario is that the upper mantle of Mars is homogeneous if GRV 99027 and other lherzolitic shergottites were delivered from various craters by individual impact events. In order to clarify these possibilities, age determinations of several crucial events of GRV 99027 must be made, including crystallization of magma, major impact related to the formation of maskelynite, and launching the rock to the Earth.

*Acknowledgments*—We are grateful to Drs. J. Bridges, T. Mikouchi, and R. L. Korotev for their constructive reviews. The sample is supplied by the Polar Research Institute of China. This work is supported by the Natural Science Foundation of China (Grant 40232026) and Chinese Academy of Sciences (Grant KZCX3-SW-123).

*Editorial Handling*—Dr. Randy Korotev

## REFERENCES

- Asimow P. D. and Ghiorso M. S. 1998. Algorithmic modifications extending MELTS to calculate subsolidus phase relations. *American Mineralogist* 83:1127–1131.
- Beck P., Gillet P., El Goresy A., and Mostefaoui S. 2005. Timescales of shock processes in chondritic and martian meteorites. *Nature* 435:1071–1074.
- Borg L. E., Nyquist L. E., Wiesmann H., and Reese Y. 2002. Constraints on the petrogenesis of Martian meteorites from the Rb-Sr and Sm-Nd isotopic systematics of the lherzolitic shergottites ALH 77005 and LEW 88516. *Geochimica et Cosmochimica Acta* 66:2037–2053.
- Boynton W. V., Hill D. H., and Kring D. A. 1992. The trace-element composition of LEW 88516 and its relationship to SNC meteorites (abstract). 23rd Lunar and Planetary Science Conference. pp. 147–148.
- Clayton R. N. and Mayeda T. K. 1996. Oxygen isotope studies of achondrites. *Geochimica et Cosmochimica Acta* 60:1999–2017.
- Delaney J. S. 1992. Petrological comparison of LEW 88516 and ALH A77005 shergottites. *Meteoritics* 27:213.
- Dreibus G., Jochum K. H., Palme H., Spettel B., Wlotzka F., and Waenke H. 1992. LEW 88516: A meteorite compositionally close to the “Martian mantle.” *Meteoritics* 27:216–217.
- Eugster O., Busemann H., Lorenzetti S., and Terribilini D. 2002.

- Ejection ages from krypton-81-krypton-83 dating and pre-atmospheric sizes of martian meteorites. *Meteoritics & Planetary Science* 37:1345–1360.
- Ghiorso M. S. and Sack R. O. 1991. Fe-Ti oxide geothermometry: Thermodynamic formulation and the estimation of intensive variables in silicic magmas. *Contributions to Mineralogy and Petrology* 108:485–510.
- Ghiorso M. S. and Sack R. O. 1995. Chemical mass transfer in magmatic processes IV: A revised and internally consistent thermodynamic model for the interpretation and extrapolation of liquid solid equilibria in magmatic systems at elevated temperatures and pressures. *Contributions to Mineralogy and Petrology* 119:197–212.
- Ghosal S., Sack R. O., Ghiorso M. S., and Lipschutz M. E. 1998. Evidence for a reduced, Fe-depleted martian mantle source region of shergottites. *Contributions to Mineralogy and Petrology* 130:346–357.
- Gleason J. D. 1997. Petrography and bulk chemistry of Martian Iherzolite LEW 88516. *Geochimica et Cosmochimica Acta* 61:4007–4014.
- Goodrich C. A. 2002. Olivine-phyric martian basalts: A new type of shergottite. *Meteoritics & Planetary Science* 37:B31–B34.
- Goodrich C. A., Herd C. D. K., and Taylor L. A. 2003a. Spinel and oxygen fugacity in olivine-phyric and Iherzolitic shergottites (abstract). 34th Lunar and Planetary Science Conference. p. 1426.
- Goodrich C. A., Herd C. D. K., and Taylor L. A. 2003b. Spinel and oxygen fugacity in olivine-phyric and Iherzolitic shergottites. *Meteoritics & Planetary Science* 38:1773–1792.
- Hale V. P. S. and McSween H. Y. 1999. A re-evaluation of intercumulus liquid composition and oxidation state for the Shergotty Martian meteorite. *Geochimica et Cosmochimica Acta* 63:1459–1470.
- Harvey R. P., Wadhwa M., McSween H. Y. J., and Crozaz G. 1993. Petrography, mineral chemistry and petrogenesis of Antarctic shergottite LEW 88516. *Geochimica et Cosmochimica Acta* 57:4769–4783.
- Head J. N. 2003. The relative abundance of recently launched meteorites from the Moon and Mars (abstract #1961). 34th Lunar and Planetary Science Conference. CD-ROM.
- Head J. N., Melosh H. J., and Ivanov B. A. 2002. Martian meteorite launch; high-speed ejecta from small craters. *Science* 298:1752–1756.
- Herd C. D. K., Borg L. E., Jones J. H., and Papike J. J. 2002. Oxygen fugacity and geochemical variations in the martian basalts: Implications for martian basalt petrogenesis and the oxidation state of the upper mantle of Mars. *Geochimica et Cosmochimica Acta* 66:2025–2036.
- Hsu W., Guan Y., Wang H., Leshin L. A., Wang R., Zhang W., Chen X., Zhang F. and Lin C. 2004. The Iherzolitic shergottite Grove Mountains 99027: Rare earth element geochemistry. *Meteoritics & Planetary Science* 39:701–709.
- Ikeda Y. 1994. Petrography and petrology of the ALH 77005 shergottite. *Antarctic Meteorite Research* 7:9–29.
- Ikeda Y. 1997. Petrology and mineralogy of the Y-793605 martian meteorite. *Antarctic Meteorite Research* 10:13–40.
- Ikeda Y. 1998. Petrology of magmatic silicate inclusions in the ALH 77005 Iherzolitic shergottite. *Meteoritics & Planetary Science* 33:803–812.
- Jolliff B. L., Zeigler R. A., and Korotev R. L. 2004. Petrography of lunar meteorite LAP 02205, a new low-Ti basalt possibly launch paired with NWA 032 (abstract #1438). 35th Lunar and Planetary Science Conference. CD-ROM.
- Kohler T. P. and Brey G. P. 1990. Calcium exchange between olivine and clinopyroxene calibrated as a geothermobarometer for natural peridotites from 2 to 60 kb with applications. *Geochimica et Cosmochimica Acta* 54:2375–2388.
- Korotev R. L., Zeigler R. A., and Jolliff B. L. 2004. Compositional constraints on the launch pairing of LAP 02205 and PCA 02007 with Other lunar meteorites (abstract #1416). 35th Lunar and Planetary Science Conference. CD-ROM.
- Lentz R. C. F. and McSween H. Y. Jr. 2000. Crystallization of the basaltic shergottites: Insights from crystal size distribution (CSD) analysis of pyroxenes. *Meteoritics & Planetary Science* 35:919–927.
- Lin Y. and Kimura M. 2003. Ca-Al-rich inclusions from the Ningqiang meteorite: Continuous assemblages of the nebular condensates and genetic link to type Bs. *Geochimica et Cosmochimica Acta* 67:2251–2267.
- Lin Y., Wang D., Miao B., Ouyang Z., Liu X., and Ju Y. 2003. Grove Mountains (GRV) 99027: A new Martian meteorite. *Chinese Science Bulletin* 48:1771–1774.
- Lin Y., Ouyang Z., Wang D., Miao B., Liu X., Kimura M., and Jun Y. 2002. Grove Mountains (GRV) 99027: A new martian Iherzolite. *Meteoritics & Planetary Science* 37:A87.
- Lindsley D. H. and Andersen D. J. 1983. A two-pyroxene thermometer. Proceedings, 14th Lunar and Planetary Science Conference. pp. 887–906.
- Lindstrom M. M., Mittlefehldt D. W., Treiman A. H., Wentworth S. J., Gooding J. L., Morris R. V., Keller L. P., and McKay G. A. 1992. LEW 88516: A new shergottite from Antarctica (abstract). 23rd Lunar and Planetary Science Conference. pp. 783–784.
- Lundberg L. L., Crozaz G., and McSween H. Y. Jr. 1990. Rare earth elements in minerals of the ALH A77005 shergottite and implications for its parent magma and crystallization history. *Geochimica et Cosmochimica Acta* 54:2535–2547.
- McSween H. Y. Jr., Stolper E., Taylor L. A., Muntean R. A., O'Kelley G. D., Eldridge J. S., Biswas S., Ngo H. T., and Lipschutz M. E. 1979. Petrogenetic relationship between Allan Hills 77005 and other achondrites. *Earth and Planetary Science Letters* 45:275–284.
- McSween H. Y. Jr., Lundberg L., and Crozaz G. 1988. Crystallization of the ALH A77005 shergottite: How closed is a closed system (abstract)? 19th Lunar and Planetary Science Conference. pp. 766–767.
- Miao B., Ouyang Z., Wang D., Ju Y., Wang G., and Lin Y. 2004. A new Martian meteorite from Antarctica: Grove Mountains (GRV) 020090. *Acta Geologica Sinica* 78:1034–1041.
- Mikouchi T. and Miyamoto M. 1997. Yamato-793605: A new Iherzolitic shergottite from the Japanese Antarctic meteorite collection. *Antarctic Meteorite Research* 10:41–60.
- Mikouchi T. and Miyamoto M. 2000. Iherzolitic martian meteorites Allan Hills 77005, Lewis Cliff 88516 and Yamato-793605: Major and minor element zoning in pyroxene and plagioclase glass. *Antarctic Meteorite Research* 13:256–269.
- Morikawa N., Misawa K., Kondorosi G., Premo W. R., Tatsumoto M., and Nakamura N. 2001. Rb-Sr isotopic systematics of Iherzolitic shergottite Yamato-793605. *Antarctic Meteorite Research* 14:47–60.
- Norman M. D. 1999. The composition and thickness of the crust of Mars estimated from REE and Nd isotopic compositions of Martian meteorites. *Meteoritics & Planetary Science* 34:439–449.
- Nyquist L. E., Bogard D. D., Shih C.-Y., Greshake A., Stöffler D., and Eugster O. 2001. Ages and geologic histories of martian meteorites. *Space Science Reviews* 96:105–164.
- Sack R. O. and Ghiorso M. S. 1991. Chromian spinels as petrogenetic indicators: Thermodynamics and petrologic applications. *American Mineralogist* 76:827–847.



- Shih C. Y., Nyquist L. E., Bogard D. D., McKay G. A., Wooden J. L., Bansal B. M., and Wiesmann H. 1982. Chronology and petrogenesis of young achondrites, Shergotty, Zagami, and ALH A77005: Late magmatism on a geologically active planet. *Geochimica et Cosmochimica Acta* 46:2323–2344.
- Treiman A. H., McKay G. A., Bogard D. D., Mittlefehldt D. W., Wang M. S., Keller L., Lipschutz M. E., Lindstrom M. M., and Garrison D. 1994. Comparison of the LEW 88516 and ALH A77005 martian meteorites: Similar but distinct. *Meteoritics* 29: 581–592.
- Wadhwa M. 2001. Redox state of Mars' upper mantle and crust from Eu anomalies in shergottite pyroxenes. *Science* 291:1527–30.
- Wadhwa M., McKay G. A. and Crozaz G. 1999. Trace element distributions in Yamato-793605, a chip off the “martian lherzolite” block. *Antarctic Meteorite Research* 12:168–182.
- Warren P. H. and Kallemeyn G. W. 1997. Yamato-793605, EET79001, and other presumed martian meteorites: Compositional clues to their origins. *Antarctic Meteorite Research* 10:61–81.
- Warren P. H. and Bridges J. C. 2005. Geochemical subclassification of shergottites and the crustal assimilation model (abstract #2098). 36th Lunar and Planetary Science Conference. CD-ROM.
- Wood B. J. 1991. Oxygen barometry of spinel peridotites. In *Oxide minerals: Petrologic and magnetic significance*, edited by Lindsley D. H. Boulder, Colorado: Mineralogical Society of America. pp. 417–431.
- Xirouchakis D., Draper D. S., Schwandt C. S., and Lanzirotti A. 2002. Crystallization conditions of Los Angeles, a basaltic Martian meteorite. *Geochimica et Cosmochimica Acta* 66:1867–1880.
- Zinner E. and Crozaz G. 1986. A method for the quantitative measurement of rare earth elements in the ion microprobe. *International Journal of Mass Spectrometry and Ion Processes* 69:17–38.
-